LUND UNIVERSITY

Large Eddy Simulation of Turbulent Reactive Flows under HCCI Engine Conditions

Joelsson, Tobias

2011

Large Eddy Simulation of Turbulent Reactive Flows under HCCI Engine Conditions

Tobias Joelsson

May 2011

Lund

Doctoral Thesis

Thesis for the Degree of Doctor of Philosophy in Engineering

ISBN 987-91-7473-174-3
ISSN 0282-1990
ISRN LUTMDN/TMHP–11/1081–SE

Division of Fluid Mechanics
Department of Energy Sciences
Faculty of Engineering–LTH
Lund University
Box 118
SE-221 00 LUND
SWEDEN

Printed by Tryckeriet i E-huset, Lund – Sweden, May 2011


See you in the Future

List of Papers

Six papers are included in the thesis. The thesis author is the first author of five of the papers, and is the second author of the sixth paper. The thesis author is responsible for the analysis and of the results that was carried out for the writing of the five papers for which he was the first author. He is also responsible for the numerical simulations part of the sixth paper, including analysis of the results and writing of the paper.

Paper 1

Joelsson T., Yu R., Bai X.S., Vressner A., Johansson B., "Large Eddy Simulation and Experiments of the Auto-ignition process of Lean Ethanol/air Mixture in HCCI Engines", **Transaction of SAE, SAE International Journal of Fuels and Lubricants,** vol.117:4, pp.1110-1119, (2009)

Paper 2

Yu R., Joelsson T., Bai X.S., Johansson B., "Effect of Temperature Stratification on the Auto-ignition of Lean Ethanol/air Mixture in HCCI Engine", **SAE paper 2008-01-1669**, (2008)

Paper 3

Joelsson T., Yu R., Sjöholm J., Tunestål P., Bai X.S., "Effects of Negative Valve Overlap on the auto-ignition process of lean ethanol/air mixture in HCCI-engines", **SAE paper 2010-01-2235**, (2010)

Paper 4

Joelsson T., Yu R., Bai X.S., Takada N., Sakata I., Yanagihara H., Lindén J., Richter M., Aldén M., Johansson B., "Flow and Temperature Distribution in an Experimental Engine: LES Studies and Thermographic Imaging", **SAE paper 2010-01-2237**, (2010)

Paper 5

Joelsson T., Yu R., Bai X.S., "Large Eddy Simulation of ignition and reaction front propagation in a spark assisted HCCI engine", **manuscript submitted to 7th Mediterranean Combustion Symposium, 2011**.

Paper 6

Joelsson T., Yu R., Bai X.S., "Large Eddy Simulation of tumble flow and turbulence in an experimental engine", manuscript to be submitted for **Journal publication**.

Abstract

Large Eddy Simulation (LES) modeling was employed here for studying homogeneous charge compression ignition (HCCI) combustion under differing engine operation and mixture conditions, including real engine configurations and generic test cases. An HCCI model developed previously was validated by comparing the simulation results with the results of the engine experiments. A new spark-assisted HCCI (SACI) combustion model was developed and was tested. The tumble flow dynamics and turbulence eddies under experimental low-speed engine conditions were simulated to enable a better understanding of engine flow dynamics to be obtained. The onset of temperature inhomgeneity was investigated systematically, the results being compared with laser diagnostic data. The ignition kernel/eddy interaction was simulated to gain insight into the HCCI ignition process under differing of turbulence conditions. HCCI combustion was found primarily to be affected by the in-cylinder temperature stratification. For a given combustion phasing, such as the crank angle at which 10% of heat has been released (CA10), both the combustion process and the pressure-rise-rate was found to be slower, when there was a large degree of stratification temperature, conditions that provided opportunity for the engine to be run under high load conditions. LES results that were obtained showed that turbulence could have an appreciated effect on the HCCI combustion process under various conditions. Under typical engine conditions, due to rapid propagation of the ignition front, turbulence is unable to affect the reaction zones directly, such as by wrinkling the reaction front or by differential diffusion that serves to adjust the radical levels. Turbulence affects HCCI combustion mainly through modifying the temperature field. It affects the process in two ways; the one is by generating temperature stratification through heat transfer between the wall and the in-cylinder gas, the other is to smear out the temperature stratification in the gas mixture through the action of turbulence eddies. If either the hot zone or the cold zone in the mixture is large in size, for example larger than the integral length scale, turbulent heat transfer may fail to smooth out the temperature stratification quickly, reducing the effect that the turbulence would otherwise have on the ignition process. If, on the other hand the scales of the hot/cold zones are small, turbulence can have a decided effect on the HCCI combustion process nevertheless. It was shown that temperature stratification in an engine is generated by means of three major mechanisms: mixing of the cold intake gas with the hot residual gas, wall-heat transfer, and compression of the mixture. The last mechanism is less well known than the other two. By having a large amount of residual gas or exhaust-gas-recirculation (EGR) in the cylinder the temperature stratification can be enhanced and thus affect the HCCI combustion process. SACI combustion is shown to be sensitive to both turbulence and temperature stratification. The operation window for SACI is narrow. If the temperature is low, the process is mainly an SI one, and if the temperature is high, it is largely a HCCI process. As a result using SACI to control HCCI engine may not be easy.

Keywords: Large Eddy Simulation, Internal Combustion Engines, In-cylinder flow, Temperature inhomogenity, Turbulent combustion, HCCI, SACI, CFD, LES

Nomenclature

Latin Characters

c	progress variable [-]
c_p	specific heat capacity [J·kg^{-1}·K^{-1}]
C_S	Smagorinsky constant [-]
D_n	thermal diffusion coefficient of species n [m^2·s^{-1}]
h	specific enthalpy [J·kg^{-1}]
ℓ_0	subgrid length scale [m]
p	hydrodynamic pressure [Pa]
P	thermodynamic pressure [Pa]
R_u	universal gas constant [J·K^{-1}·mol^{-1}]
S	characteristic rate of strain
S_{ij}	rate of strain tensor [s^{-1}]
t	time [s]
t_0	turbulent integral time scale [s]
t_η	Kolmogorov time scale [s]
T	temperature [K]
u, v, w	velocity components [m·s^{-1}]
u'	velocity fluctuation [m·s^{-1}]
u_η	Kolmogorov velocity scale [m·s^{-1}]
u_Δ	turbulence subgrid scale velocity [m·s^{-1}]
x, y, z	space coordinates [m]
Y	mass fraction [-]
W	molecular weight [kg·mol^{-1}]

Greek Characters

α	heat diffusivity [m^2·s^{-1}]
δ_{ij}	Kronecker delta [-]
Δ	LES filter width [m]
ε	dissipation rate [J·s^{-1}·kg^{-1}]
ζ	WENO optimal weight [-]
η	Kolmogorov length scale [m]
λ	thermal conductivity [W·K^{-1}·m^{-1}]
λ_t	Taylor length scale [m]
ξ	Moving grid coordinate in x-direction [m]
μ	dynamic viscosity [kg·m^{-1}·s^{-1}]
ν	kinematic viscosity [m^2·s^{-1}]
ρ	density [kg·m^{-3}]
τ_{ij}	viscous stress tensor [m^2·s^{-2}]
τ_{ij}^R	subgrid scale stress tensor [m^2·s^{-2}]
ϕ	arbitrary variable [-]
φ	equivalence ratio [-]
χ	scalar dissipation rate [s^{-1}]
$\dot{\omega}$	reaction rate [kg·m^{-3}·s^{-1}]
Ω_{ij}	rate of rotation tensor [s^{-1}]

Non-Dimensional Numbers

Reynolds number $\mathrm{Re} = \dfrac{uL}{\nu}$

Prandtl number $\mathrm{Pr} = \dfrac{\nu}{\alpha}$

Lewis number $\mathrm{Le}_n = \dfrac{\alpha}{D_n}$

Schmidt number $\mathrm{Sc}_n = \dfrac{\nu}{D_n}$

Mach number $\mathrm{Ma} = \dfrac{u}{c}$

Abbreviations

AI	Auto-Ignition front
ATAC	Active Thermo-Atmosphere Combustion
BML	Bray-Moss-Libby
CAD	Crank Angle Degree
CCV	Cycle-to-Cycle Variation
CeCOST	the Centre for Combustion Science and Technology
CFD	Computational Fluid Dynamics
CFL	Courant-Friedrichs-Levy condition
CH_2O	Formaldehyde
CHO	Formyl radical
CI	Compression Ignition
CO	Carbon monoxide
CO_2	Carbon dioxide
DES	Detached Eddy Simulation
DNS	Direct Numerical Simulation
EGR	Exhaust Gas Recirculation
HC	Hydrocarbons
HCCI	Homogenous Charge Compression Ignition
HO_2	Hydroperoxy radical
IC	Internal Combustion
IEM	Interaction by Exchange with the Mean
KC-FP	KompetensCentrum FörbränningsProcesser a.k.a Competence Center Combustion Processes - CCCP
LES	Large Eddy Simulation
NO	Nitrogen monoxide
NO_2	Nitrogen dioxide
NO_X	NO + NO_2
NVO	Negative Valve Overlap
MPI	Message Passing Interface
O	Oxygen atom
O_2	Oxygen gas
OH	Hydrogen monoxide, Hydroxyl radical
PCCI	Premixed Charge Compression Ignition
PDF	Probability Density Function
PF	Premixed Flame front
PLIF	Planar Laser Induced Florescence
PRF	Primary Reference Fuel
RANS	Reynolds Average Navier-Stokes
rms	root mean square
rpm	rounds per minute
SACI	Spark Assisted Compression Ignition
SAE	Society of Automotive Engineers
SFS	Sub-Filter Scale
SGS	Sub-Grid Scale
SI	Spark Ignition
SSM	Scale-Similarity Model
TDC	Top Dead Center
UHC	Unburned Hydrocarbons
URANS	Unsteady Reynolds Average Navier-Stokes
WENO	Weighted Essentially Non-Oscillatory

Table of Content

Chapter 1 Introduction to HCCI combustion

1.1 Principles of HCCI Engines

Homogenous-Charge-Compression-Ignition (HCCI) engines have the potential of being able to achieve simultaneously both high degree of engine efficiency and a low level of emission of such pollutants as NO_X and soot. This has attracted the attention both of engine industry and of academic researchers in this area worldwide, for furthering the efforts of each to develop and optimize engine performance and gain a understanding of the physical and chemical processes involved. HCCI makes use of basic elements of both compression-ignition (CI) and spark-ignition (SI) engines. In HCCI engines the fuel and air are premixed prior to entering the combustion chamber, in a manner similar to that of an SI engine. The mixture in the engine cylinder is then auto-ignited by compression, just as it is in a CI engine. These two characteristics together enable HCCI engines to operate at a high compression ratio and to thus achieve a high degree of engine efficiency. HCCI engines can operate under rather fuel-lean conditions. This results in a large reduction in the formation of soot and of thermal NO during the combustion process [1-4].

Ideally, ignition in a homogeneous charge would occur homogenously in the combustion chamber as a whole, chemical kinetics dictating the course of the combustion process. Numerical simulations based on chemical kinetics alone, however have failed to reproduce various experimental observations, such as those regarding the pressure-rise-rate during the combustion stroke. Laser diagnostic experiments [5] have shown there to be a rather inhomogeneous distribution of ignition kernels, the reaction fronts being propagated locally in space. The geometry of the reaction fronts is rather irregular, indicating a significant effect of turbulence [6-8].

Since the charge cannot be perfectly mixed and cannot be heated up uniformly during the compression stroke, it auto-ignites, almost simultaneously in a number of small spots within the combustion volume. The combustion spots then either propagate to the mixture found in the immediate vicinity or trigger ignition of the mixture in differing locations. Such behavior can result in the combustion phasing and duration of combustion considerably differing from cycle to cycle. Too short a duration of combustion results in a very high pressure-rise-rate and in rapid heat release within the engines cylinder, creating problems of knocking. Since HCCI engines usually run on a very lean or diluted fuel/air mixture, knocking is usually not a significant problem there, although a high pressure-rise-rate can result in a high noise level.

There are additional uncertainties regarding the control of combustion by auto-ignition spots in an internal combustion engine. In particular, it is very difficult to obtain the same charge distribution in different cycles since the onset of ignition and the exact position of it in time and space can vary from cycle to cycle. This very considerable variation in ignition timing results in large in-cylinder variations in pressure, which leads to still larger variations in combustion phasing.

Spark-ignition can be used to control the ignition timing (and combustion phasing) in HCCI engines. A portion of the reactants in the cylinder is burned by a spark-initialized premixed flame. The ongoing combustion, together with the continuous increase in the in-cylinder pressure, lead to still higher temperatures. When the charge temperature reaches a critical level, the fuel auto-ignites and the remaining reactants contained in the system being

consumed. This process is referred to as spark assisted HCCI, also known as Spark-Assisted-Compression-Ignition (SACI) [9].

Emissions of soot and NO_X in HCCI engines generally remain low due to HCCI combustion running on a fuel lean charge. Accordingly, the overall mean temperature tends to remain below the NO peak formation-temperature level, as can be seen in figure 1. However, when the lean-burning or highly diluted mixture drops in temperature too rapidly in the later stages of the combustion stroke, it can cause serious problems of emissions, which can contain large amounts of unburned hydrocarbon molecules and CO.

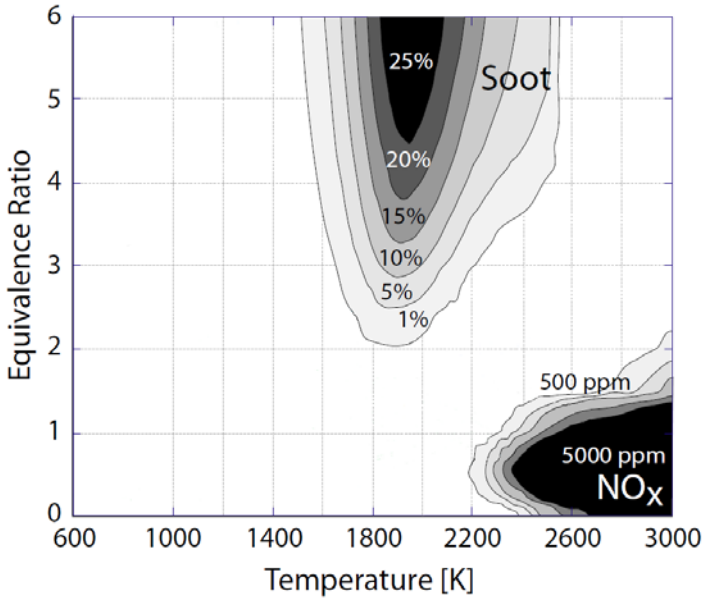

Figure 1: ϕ -T diagram of Diesel fuel combustion, showing Soot and NO_X formation regions [10].

There are many parameters that can affect the performance of HCCI engine such as engine speed, fuel dilution, and the compression ratio. For an HCCI engine to perform optimally, sophisticated control of various parameters would be needed. It has been found for HCCI engines, for example, that when the amount of fuel provided is decreased, an increase in engine speed increases operational range of the machine [10]. During the past 30 years or so, continuous efforts have been made by engineers and researcher to develop highly efficient, reliable and clean HCCI engines [11].

1.2 The Development of HCCI Engine

HCCI combustion was first described by Onishi et al. in 1979 [12] and Noguchi et al. [13] later that year. HCCI combustion was there compared with SI combustion in a 2-stroke SI-engine. It has been shown by high-speed schlieren photography that HCCI combustion has quite a different reaction zone structure than SI combustion does. In SI combustion, a thin but distinct reaction zone propagates from the spark site to the cylinder as a whole, whereas it has been shown that in HCCI combustion, an ignition reaction process takes place in the entire cylinder [12]. Noguchi et al. [13] studied the onset of auto-ignition in a two-stroke optical HCCI engine (which they termed an Active Thermo-Atmosphere Combustion engine, ATAC) by the imaging of CHO, HO_2, OH, and O radicals. They noted that the CHO, HO_2 and O radicals appeared earlier than the OH radicals did, indicating the effects of low-temperature chemistry in the course of the combustion process. Later on, in 1983 Najt and Foster [14] studied the functioning of an HCCI motor having a 4-stroke engine configuration, a preheated air inlet and EGR control.

By 1995, some 10 papers on HCCI engines had been published, as summarized by Hultqvist [15]. Early studies in this area were concerned with such matters as effects of fuel selected, the wall temperature, the equivalence ratio, the delivery ratio and engine speed e.g. (Iida et al. [16-19]), of throttling of the transfer port, (Duret et al. [20]), and of further operating parameters on engine performance. It was generally found that use of HCCI in two-stroke engines improved engine efficiency, although minor problems connected with unburned hydrocarbons and CO were encountered.

Since 1996 HCCI combustion has attracted the attention of further research groups, the number of papers published on HCCI engines having grown rapidly [15]. The work of Christensen et al. [21-25] on experimental engines of different types is a good example of the systematic studies that have been carried out, aimed at obtaining a better understanding of the basic operating parameters and of the fuels employed (e.g. natural gas, ethanol, iso-octane and primary reference fuels (PRF), as well as mixtures of iso-octane and n-heptane) in the operating range of HCCI engines. Much of Christensen's work can be found in his thesis [26] which includes 25 published papers together with others. Christensen et al. [27, 28] were also the first to note the significant effects of piston geometry on the ignition timing and duration of combustion in HCCI engines. These observations led to the speculation that turbulence can play an important role in HCCI combustion. Several researchers have attempted to simulate the process numerically, in efforts to better understand the effects of piston geometry on the HCCI combustion (e.g. Kong et al. [29], and the work of the present thesis, Paper 1).

Thanks to the support of the Swedish engine industry and the government funding agency, STEM, systematic research on HCCI engines has been carried out at Lund University's Engineering Faculty - LTH [9, 15, 26, 30-38], Chalmers University of Technology - CTH [39-50] and KTH - Royal Institute of Technology [51-57]. The well-documented knowledge of engine performance under different conditions, such as those of EGR, fuels, injection strategies, variable compression ratios, loads, charge stratification, turbocharge, etc. employed has laid the foundations for designing future high performance engines.

Significant contributions have been made during the past decades by researchers in various part of the world, as is discussed later on in the thesis and in the papers contained in the appendix. A comprehensive recent review on HCCI engines can be found in papers by Dec et al. [58-60] and Yao et al. [61].

1.3 Fundamental Physics involved in HCCI combustion

In order to be able to optimize the many parameters that affect HCCI combustion, it is important that one understands the basic physics of HCCI engines. The following physical processes, similar to those occurring in SI and CI engines take place in HCCI engines.

First, the key process of the mixing of the fuel, the air and, either the EGR or the residual gas remaining from previous cycles occurs. Even in port-fuel injection there is a slight inhomogeneity of the fuel/air mixture. Richter et al. [62] measured the distribution of fuel in the cylinder on the basis of the PLIF of the fuel tracer (acetone) employed. The fuel was injected in two different ways: The one way was to inject it into the intake port in an unmixed state, the fuel beginning to mix with the air there. The other way was to inject the fuel and air into the cylinder after premixing them in a mixing tank. They found port-fuel injection to lead to certain inhomogeneity in the composition of mixture as compared with the premixing tank case.

Secondly, a heat transfer process within the cylinder, associated with the mixing of the mass the cylinder contains take place. The wall exchanges heat with the gases in the boundary layer of the wall; the flow occurring, which typically is turbulent, enhances both the mixing of the

gases and exchange of heat that takes place in the bulk flow. A temperature stratification develops in the cylinder due to the differences in temperature between the intake gas, the EGR/residual gas and the wall.

Third, a chemical reaction which is a key process occurring in HCCI engines takes place. This chemical reaction dictates the onset of ignition of the charge and the propagation of ignition fronts within the cylinder. Subsequently, it also affects such matters as the phasing, and the duration of combustion, the rate of increase in pressures, and the noise level.

The interplay of these different processes involved, determines the performance of the HCCI engine. The role each of these processes plays effects to the results obtained depend upon the engine parameters and the operating conditions. Although it is well recognized that the ignition process in HCCI engines is basically governed by the chemical kinetics involved [14, 63], turbulence also plays an important role there. Where and when ignition starts is affected by the mixing of the fuel and air, by the EGR and the heat transfer caused by turbulence in the cylinder prior to the onset of ignition. The ignition sites in HCCI engines are not homogeneous, due to the inherent inhomogeneity of the temperature or the composition or both. Richter et al. [62] and Hultqvist et al. [64] conducted LIF measurements of the fuel tracer employed (acetone) and of the combustion intermediates, CH_2O and OH radicals, found in several optical engines. They found it to be typical of HCCI combustion for ignition to first occur at various random sites, and this is to be followed by rapid propagation of the flame front, regardless of whether the fuel is injected into the intake port without its first being mixed with air or instead is premixed with air in a mixing tank prior to it is being injected into the cylinder.

The mechanisms of reaction front propagation in a mixture of homogeneous composition but showing temperature stratification have been studied by a number of authors earlier [65-69]. Initial work in this area was conducted by the Russian scientists in the 1930s to the 1960s (see Zeldovich [65] for a review). On the basis of theoretical studies he conducted concerning the propagation of reaction fronts in an idealized one-dimensional infinitely long domain, Zeldovich [65] described three distinct mechanisms of reaction-front propagation in a homogeneous mixture having a non-homogeneous initial temperature: *detonation*, *deflagration*, and *spontaneous propagation*.

Detonation leads to engine knock that should be avoided; it can occur for example, in a homogeneous mixture having a temperature gradient of very small size. *Deflagration*, or front propagation (also known as flame propagation) is controlled by both chemical reactions and the diffusion of heat and mass between the reaction front and the unburned mixture. *Spontaneous propagation*, in turn is due to the difference between adjacent points in ignition delay time.

Two of the three mechanisms referred to above that are responsible for reaction-front propagation have been identified, for a constant volume under HCCI condition, by use of two-dimensional Direct Numerical Simulations (DNS) of a lean hydrogen/air mixture [68]. The first mechanism is spontaneous ignition-front propagation, which is ascribed to mixtures having either a very low temperature gradient or a very lean fuel/air ratio. This is the most common mechanism for HCCI front propagation, it is accounting for about 80% of the total heat release. The second mechanism is deflagration-front propagation controlled both by reaction and by diffusion. Turbulence can interact with the flame front directly by wrinkling it and by enhancing the transfer of mass and heat between the preheated zone and the reaction zone.

Under conditions of constant volume or of piston compression, ignition front propagation is strongly coupled with the rise in pressure. The early ignition of a 'hot spot' leads to a rise in the overall cylinder pressure. This affects the auto-ignition that takes place in the cooler zones, and thus propagation of the spontaneous ignition front as well. A detailed understanding of

this is helpful in developing high fidelity simulation models. The modeling of HCCI combustion can be simplified appreciably for example by neglecting the deflagration front propagation in the cylinder that occurs. This has led to the development of single-zone, two-zone and multiple-zone models [63, 66, 70-72]. In using a two-zone model, Hajireza et al. [66] found that even a small difference within the initial temperature field can grow rapidly as the mixture is auto-ignited, a development which promotes a temperature gradient that can strongly affect propagation of the deflagration front [69]. A recent numerical calculations of the iso-octane ignition that can occur in a pressure counterflow configuration under atmospheric conditions indicated that, as the temperature gradient in a mixture is built up, the overall ignition characteristics are strongly affected by the mixing rate [67].

1.4 Parameters affecting HCCI combustion

Wide varieties of parameters affecting HCCI engine performance have been studied thus far. The geometry of the combustion chamber, the temperature of the intake gas and of the coolant, fuel properties, fuel-injection strategies, EGR, load/equivalence ratios, compression ratios, the in-cylinder flow swirl and intake/exhaust valve timing are a few examples of the many governing parameters that can be applicable.

Cylinder geometry has been found to strongly affect the HCCI combustion process. Systematic experimental investigations have been carried out to better understand the effect of piston geometry, first by Christensen et al. [27, 28] and later by Vressner et al. [73, 74] together with Seyfried et al. [75]. In these two studies referred to, an optical engine in which two different piston geometries were used was employed. The one of these was a flat disc shaped piston, normally used in optical engines for achieving maximal optical access, and the other was a dished square bowl shaped piston. In the later study both cycle-resolved chemiluminescence imaging [73] and PLIF of fuel tracer (acetone) [75] measurements were carried out. It was found that use of the square-bowl shaped piston provided a prolonged combustion duration for the HCCI combustion relative to the engines with a flat disc shape piston.

It was also of interest to investigate how the piston material affects the duration of combustion. Experiments were conducted by using both disc-shaped and square-bowl-shaped pistons, both of them made of quartz glass and metal. It was found that the completely metal engines were difficult to auto-ignite, probably due to quenching [74]. Under conditions similar to those present in the optical engines, square bowl metal engine was shown to have a shorter combustion duration than that of quartz-glass square-bowl engine did. To understand why this is happening a systematic LES study has been carried out in Paper 1 and [76].

HCCI engines running at low load levels show high levels of CO and HC emissions. A possible method of overcoming this problem, without losing too much in the way of efficiency, is use of charge stratification. This technique has been shown to result in a lowering of CO and HC emission levels without much of a decrease in efficiency [58].

SI and HCCI can be combined so as to achieve a high level of engine efficiency and a low noise level. The HCCI mode, with its greater efficiency, can be used towards the lower end of the load range of the SI engine so as to improve the efficiency of the SI engine. The SI mode, in turn, can be used at higher load. Increasing the charge temperature in an SI-engine prior to compression enables an HCCI mode to be achieved if small mechanical modifications are made. This can be accomplished by preheating the inlet air. Another way of increasing the charge temperature is to reuse the exhaust gas and let it be recirculated back into the inlet and be used then in the cycle thereafter. Employing this recirculation strategy, termed exhaust-gas-recirculation (EGR), makes it possible to maintain a high charge temperature and thus to lengthen the operational regime [77].

One can also achieve result similar to that obtained by use of exhaust gas recirculation through the inlet by keeping the residual gas within in the cylinder and only having fresh charge in the inlet ports [35]. This functions in a manner similar to that of a commercial engine system which utilizes the breathing mechanisms of the engine to trap hot residual gas inside the cylinder during the exhaust and intake strokes, it is then serving as an inert gas within the cylinder. This can be done by introducing a negative-valve-overlap, NVO, provided with exhaust-valve-closing, EVC, in front of the inlet-valve-opening, IVO, and keeping both of them closed for a period of time. Use of NVO makes it possible to trap a certain amount of residual gas within the cylinder so as to increase the in-cylinder temperature. The trapped residual gas also reduces the pump losses, extremely important for SI-engines [78]. NVO-HCCI can be achieved by application of the NVO principle [79]. This mode was tuned such that burning occurred under lean conditions in which there were sufficient residuals to heat the charge to auto-ignition level but diluted to the range where the NO_X are kept in low levels. Other emission species such as HC and CO increased due to the fuel being partly oxidized [9].

1.5 Scope of the Thesis

It has been hypothesized that inhomogeneity of temperature field is the major factor leading to the onset of inhomogeneous ignition kernels, since the chemical reactions involved are strongly temperature dependent. Turbulence is assumed to only be responsible for inhomogeneity in temperature at the level of a large integral length scale, through its transporting heat from the walls to the bulk flow. There is minor interaction between small scale turbulence eddies and the ignition kernel that are present. These relationships have led to the development of several models aimed at accounting for the spatial temperature inhomogeneity, which is present. Kraft et al. [70] suggested use of a stochastic reactor model. At the time, flow was still being modeled as taking place within a single zone. They assumed species concentrations and temperature to vary randomly in space. They described molecular diffusion induced by turbulent mixing in terms of an IEM (Interaction by Exchange with the Mean) model. They found predictions of CO production and of unburned hydrocarbons with use of this model to be better than with use of the single-zone model. The IEM model failed to adequately predict, however the duration of experimentally observed combustion under conditions of high turbulence. Multiple zone models developed by Aceves et al. [63, 71] and by Flowers et al. [72], are able to take account of a certain degree of spatial inhomogeneity in temperature. In multi-zone models, the flow motion is typically simulated by use of CFD codes taking account of k-ε turbulence closure, the chemistry being resolved with use of much coarser zones than the CFD grid provides, typically ten zones altogether. Simulations with use of ten zones for the chemical kinetics were found to yield more adequate results than obtainable by use of single zone models. However, predictions of the quantities combustion products, such as of CO, produced were found to be an order of magnitude lower than the amount found on the basis of experiments [63, 71, 72]. This indicated that a large number of zones are needed in order to adequately predict detailed emissions. This suggests that micro-scale turbulence may have a major impact on the HCCI combustion process. Currently, there is no model that can accurately predict the effects of turbulence on the HCCI combustion process.

In the thesis, certain highly important, as yet unresolved issues in regard to HCCI combustion are investigated. These include the structure and the dynamics of the chemical reaction fronts there, the effects of turbulence eddies on these fronts and modeling of the combustion process. The general aims here are to obtain an increased understanding of the basic HCCI combustion process and to improve the existing numerical simulation models. A more specific goals of the project reported on are:

- To scrutinize certain major aspects of HCCI combustion, in particular the effects of turbulence in micro-scale eddies on the onset and the development of ignition kernels. The frequently employed assumption in current models is that turbulence has only a minor effect on the ignition kernels is to be examined critically, careful account being taken to the detailed structure and the dynamics of the ignition kernel.

- Another specific goal is to develop a numerical simulation model that can adequately account for the effects of turbulence on the HCCI combustion process. This is crucial for the future development and design of HCCI engines.

High fidelity numerical methods are to be used for simulating at a rather detailed level HCCI ignition, reaction front propagation, in-cylinder turbulent flows and heat transfer processes, Large Eddy Simulation (LES), in particular, being made use of. LES is a usable method for studying flow and combustion, use being made of Reynolds numbers aimed at being as realistic as possible and providing a relatively detailed spatial and temporal resolution. Eddy scales larger than Taylor micro-scales are resolved by use of LES, making it possible to simulate interactions between various large and turbulent eddies as well as chemical reactions at the ignition fronts created, and making it possible also to model eddies smaller than those on sub-grid. Ignition of the fuel/air mixture in a typical HCCI engine starts at a temperature of 600 – 1000 K and a pressure of 15 – 30 bar. The ignition delay time of a typical fuel (such as a mixture of iso-octane and n-heptane) in an HCCI engine is one of milliseconds. In the LES of an entire engine cylinder, a typical time step used is one of about 0.01 milliseconds, sufficient to resolve the ignition process.

Although the thesis is limited to numerical studies, attempts have made to couple the numerical studies to engine experiments. This has been done by collaboration with the experimentalists within the competence center for combustion process (KC-FP) at Lund University. This has resulted in joint papers, such as Papers 1, 3 and 4 in the appendix.

The remaining sections of the thesis are structured as follows. In chapter 2, a mathematical and physical account of the flow and the combustion processes in HCCI engines is provided. In chapter 3, the LES approach to studying flow and combustion in an engine is described. This is followed in chapter 4 by a brief presentation of the numerical methods used in this thesis. In chapter 5, a summary of the main results obtained in the thesis is presented. Further details concerning the results are provided in the papers included in the appendix. In chapter 6, the conclusions drawn and the perspective for future work are discussed.

Chapter 2 Physical and Mathematical Description of HCCI Combustion

2.1 Engine Cylinder Flow

Large-scale flow structures in an engine cylinder are usually described as being swirl, tumble or squish flows. Swirl is commonly defined as a controlled large-scale flow structure located parallel to the cylinder axis [1]. It is created by changing the angles of the inlet-channels in relation to the cylinder, angles which give the intake flow an initial angular momentum, figure 2. Swirl generally takes place during compression, combustion and the expansion phases that occur. Swirl-flow motion serves to generate large-flow scale structures, and to maintain them at high levels during the combustion phase. The occurrence of swirl flow increases, the level of turbulence found prior to combustion. Swirl flow can be used in standard CI-engines to enhance mixing of the spray with air. In SI-engines it also serves to increase the wrinkling of the flame surface and to enhance turbulent flame propagation [3, 80].

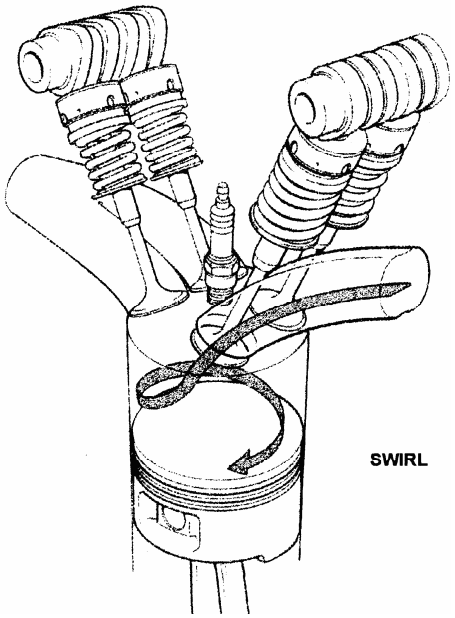

Figure 2: Schematic illustration of engine swirl flow [80]

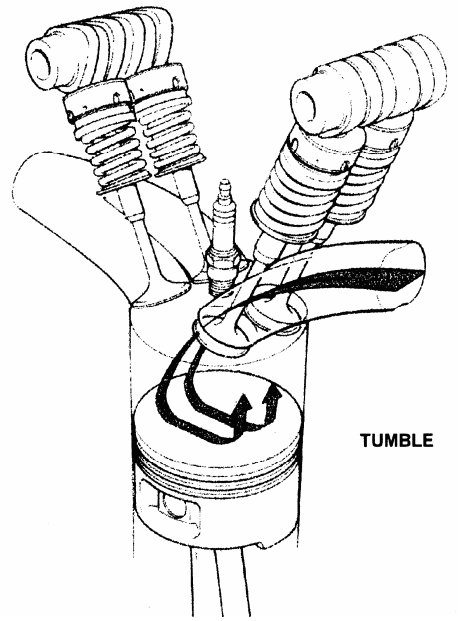

Figure 3: Schematic illustration of engine tumble flow [80]

Tumble flow is another large-scale in-cylinder flow structure, one which is generated by inlet-channel configurations, figure 3. In contrast to swirl flow, the rotational axis of tumble flow is perpendicular to the cylinder axis [3, 80]. Tumble motion creates large-scale flow motion during the intake stroke. It then continues to exist within the cylinder space, until late in the compression stroke, when it breaks up into several small scales eddies. The marked increase in turbulence close to top-dead-center (TDC) makes it especially suitable for SI-engines.

Squish flow is another large-scale flow motion, one which is generated by changes in the piston volume. Squish flow is an inward gas-flow motion having either a radial or a transverse direction relative to the piston axis. It takes place near the end of compression stroke when the outer portions of the engine have a volume much smaller than that of the central portions. Squish flow is visualized in figure 4, by use of streamlines that show the flow direction upwards to the piston bowl. Such large-scale flow motion is affected by the geometry of the combustion chamber [1].

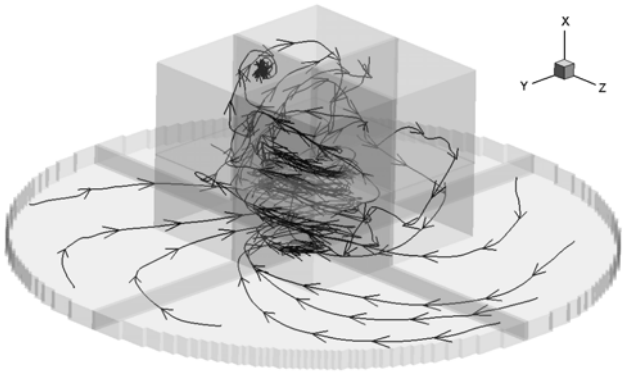

Figure 4: A squish flow structure, shown by instantaneous streamlines for engine-LES, having a square bowl shaped piston at 350 CAD, Paper 1

2.2 Turbulent Flow in the Cylinder

In-cylinder flow in an HCCI engine is almost always turbulent. The turbulence affects the heat transfer and the mixing of fuel, air and EGR, as well as the combustion process. The turbulence generated in the engine cylinder can be created by a number of different factors. It is generated above all in the shear layers of the intake flow. Motion of the piston can change the shear flow markedly and can both introduce and enhance instabilities in the flow. Gas exchange through the exhaust valves can also introduce turbulence into the system. In addition , the cylinder walls can serve to generate turbulence in the boundary layer.

Turbulent flows can be characterized by the Reynolds number as defined in (2.2.1) [81, 82]. Here u is the characteristic velocity of the system, L is the length scale of the system, and ν is the molecular kinematic viscosity of the fluid.

$$\mathrm{Re} = \frac{uL}{\nu} \tag{2.2.1}$$

The Reynolds number represents the ratio of the inertial convective forces to the viscous forces present. When the Reynolds number is small, viscous forces tend to dampen instabilities caused by the inertial forces. When the Reynolds number exceeds its critical value, the flow tends to change character and become turbulent.

2.2.1 Phenomenological Description

Describing turbulence in a precise way is difficult since it exhibits highly varying characteristics. One can better describe it in terms of certain general characteristics [83]. In the following, a brief summary of the general characteristics of turbulence is provided.

- *Three dimensional rotational structures*. Turbulence can be characterized as representing three-dimensional rotational structures of varying size, which are also known as the eddies. Eddies interact with one another through their vortexes stretching, bending and the like. In piston engines, the compression and expansion of the cylinder volume affects the stretching of the vortex, which can enhance the interaction of eddies.

- *Continuum*. The size of the smallest eddies in the engine cylinder is several order of magnitude larger than that of the mean free path of the molecules involved. Turbulence is usually assumed to take place in a continuous medium.
- *Irregular*. The structures and quantities involved in turbulent flow appear to be highly random, both in time and space.
- *Diffusive*. Turbulence enhances the transfer of mass, momentum and heat by eddy interactions.
- *Dissipative*. One speaks of different scales of turbulence. On the smallest turbulence scale, known as the Kolmogorov scale, kinetic energy is dissipated into heat. The kinetic energy on larger turbulence scale is transformed into heat through eddy interaction on smaller turbulent scales.
- *Large Reynolds Number*. Turbulence is most likely to occur when the Reynolds number is large, the range in size of the eddies involved depends very much upon the Reynolds number, higher Reynolds numbers tending to result in smaller eddies.
- *Flow*. Turbulence is a property of flow, not of fluidity.

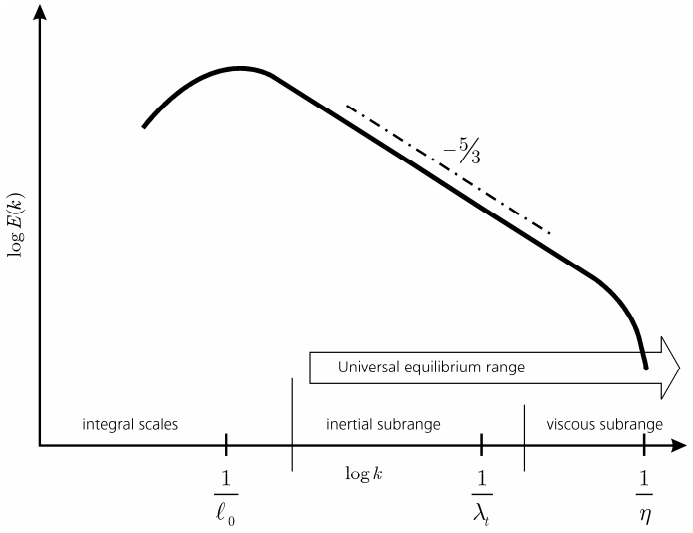

Figure 5: Turbulent Energy Spectrum

2.2.2 Scales of Turbulence

The turbulence found at any given moment in an IC engine consists of three dimensionally unsteady random eddies that vary considerably in length, time and velocity. Large-scale eddies tend to be highly anisotropic. The size of large eddies is affected by the geometry of the engine cylinder. Smaller eddies, on the other hand, according to Kolmogorov's hypothesizes of local isotropy [84], are locally isotropic, seen in statistical terms, in flows involving high Reynolds numbers. According to Pope [8] eddies smaller than one sixth the size of the large energy-containing eddies are already rather isotropic.

Figure 5 shows schematically the spectrum of turbulent kinetic energy as a function of the wave number, which can be qualitatively interpreted roughly as representing the inverse of the length scales of the turbulence eddies found. Large low-frequency eddies contain a greater amount of energy than smaller, high-frequency eddies. The large eddies are referred as energy-containing eddies. The smallest eddies are so short in length that viscous forces play as strong role as the inertial forces, the Reynolds numbers applying on the smallest eddies thus being in the order of unity. The scale involved is known as the Kolmogorov scale [84, 85]. Eddies smaller than the Kolmogorov scale cannot survive long, since they are dissipated quickly by the viscous forces which are present.

Integral scale

One can quantify large-scale energetic eddies in terms of the energy spectrum, through defining an integral length-scale that represents the size of large eddies. The integral length scale in a homogenous and isotropic turbulent case involving a zero mean velocity can be defined by use of an auto-correlation function

$$f(r) = \frac{\overline{u'(x)\,u'(x+r)}}{\overline{u'(x)\,u'(x)}} \tag{2.2.2}$$

where $u'(x)$ is the fluctuation in velocity at a given point x in space and r is the distance from this point. The integral length scale can be defined as by use of equation (2.2.2) and integration over the entire space,

$$l_0 = \int_0^\infty f(r)dr, \quad t_0 = \frac{l_0}{u'} \tag{2.2.3}$$

The integral l_0 here represents the mean distance for which the velocity fluctuations are correlated. As can be seen in equation (2.2.3) a time scale is also defined, in which the velocity of the large scale eddies is of the order of the root mean square of velocity fluctuation.

Figure 6 shows measurements on integral scales that were made in a 1.6 liter engine [86]. As can be seen, the measurement vary on an integral scale between 15 and 20 mm. Close to TDC (0 CAD) follows the measurements to follow the clearance height, i.e., are limited by the clearance height.

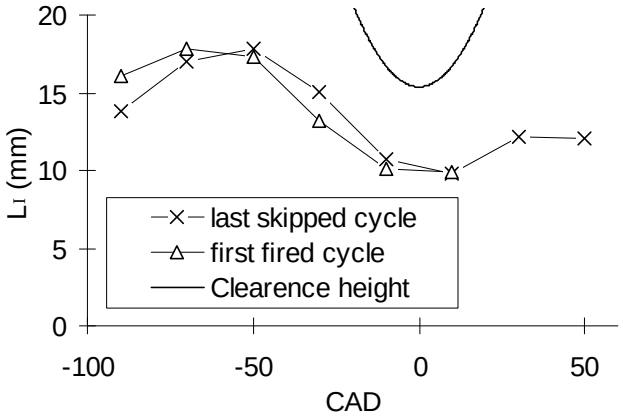

Figure 6: Measured integral length scales, showing both combustion and motored cycles, in a 1.6 liters engine cylinder. The clearance height between the cylinder head and the piston can be seen as the parabolic shape in the figure [86].

Universal equilibrium range, Inertial subrange and Taylor scale

From Kolmogorov's first similarity hypothesis, if Reynolds numbers is sufficiently high, there is a universal equilibrium range between the integral scale eddies and the smallest eddies present, within these range the statistics of motion of the turbulence eddies having a universal form that is uniquely determined by the viscosity and the dissipation rate of the turbulent kinetic energy. This is often referred to as the universal equilibrium range, which can be subdivided into two subranges. In the first subrange, the inertial subrange, the statistics of the eddies present depends, in accordance with Kolmogorov's second similarity hypothesis, on the dissipation rate ε, but is independent of the viscosity. The second subrange, between the inertial subrange and the Kolmogorov scale, is known as the dissipation range.

The Taylor length scale λ_t is a typical length scale representing the inertial subrange. By use the autocorrelation function, shown in equation (2.2.2) the second derivative at r=0, λ_t can be defined as

$$\lambda_t^2 = \frac{-2}{\left.\frac{\partial^2 f}{\partial r^2}\right|_{r=0}} \tag{2.2.4}$$

Viscous subrange and Kolmogorov scale

The viscous subrange involves the viscosity dependent region of the universal equilibrium range. In the viscous subrange turbulence eddies are assumed to follow Kolmogorov's first similarity hypothesis. The eddies on the Kolmogorov scales are determined by the viscosity υ and the dissipation rate ε. Dimensional analysis by use of Kolmogorov's three scales, length η, time t_η and velocity u_η, can be presented as follows

$$\eta \equiv \left(\frac{\nu^3}{\varepsilon}\right)^{\frac{1}{4}}, \quad t_\eta \equiv \left(\frac{\nu}{\varepsilon}\right)^{\frac{1}{2}}, \quad u_\eta \equiv \frac{\eta}{t_\eta} = (\nu\varepsilon)^{1/4} \tag{2.2.5}$$

$$\frac{\eta}{l_0} \sim \mathrm{Re}^{-\frac{3}{4}}, \quad \frac{\tau_\eta}{\tau_0} \sim \mathrm{Re}^{-\frac{1}{2}} \tag{2.2.6}$$

2.2.3 Statistical Descriptions of In-cylinder Turbulence

Since turbulence is a random process, it is convenient to introduce statistical approaches in analyze its properties. Several different methods can be used for analyzing in-cylinder turbulence [8].

Time-Averaging

Time averaging is commonly used in analyzing statistically stationary processes. A time-average can be defined as,

$$\bar{\phi} = \lim_{T\to\infty} \frac{1}{T} \int_T \phi \, dt \tag{2.2.7}$$

where ϕ is a random variable and T is the averaging time. In-cylinder turbulence is typically not a statistical stationary process. The piston motion results in the flow and the thermodynamic variables being to a marked degree a function of the piston position and thus very much a function of time. If the scale values for the energy-containing eddies are clearly distinct from values obtained for the unsteadiness caused by the piston motion, it can be sensible to decompose the solution into a slowly evolving mean flow field (effects of the piston motion) and a superimposed rapidly fluctuating component representing turbulence. In such cases, Unsteady Reynolds Averaged Navier-Stokes (URANS) can be used for engine in-cylinder flow simulations.

Space-Averaging

For homogeneous turbulence, it is convenient to make use of space averaging. A space-average can be defined as

$$\tilde{\phi} = \frac{1}{V} \int_V \phi \, dV \tag{2.2.8}$$

where V is the averaging volume. In-cylinder turbulence generally does not involve there being a homogeneous turbulence process. According to Kolmogorov's hypothesis on local isotropy, those eddies that are appreciably smaller than the energy containing eddies, for example those having one sixth or less the value of the integral scale eddies that are found are statistically isotropic[8]. This makes it sensible to make use of the space-averaging method for filtering out the small eddies. The size of the average volume need to be less than that for the energy-containing eddies since these are rather anisotropic. This is the large eddy simulation approach to be discussed later in the thesis.

Ensemble-Averaging

Ensemble averaging can be used for analyzing either statistically stationary or statistically non-stationary processes. It is appropriate to use this for characterizing in-cylinder turbulence properties over a series of cycles. An ensemble average can be defined as follows, where N is the total number of samples considered:

$$\langle \phi \rangle = \frac{1}{N} \sum_{n=1}^{N} \phi_n \tag{2.2.9}$$

Phase-Averaging

Phase-averaging can be applied to periodic processes, it is being suitable for analyzing engine in-cylinder flows. A phase-average applied to in-cylinder flows in an engine can be defined in a way similar to that of a cycle based ensemble average

$$\hat{\phi} = \frac{1}{N} \sum_{n=1}^{N} \phi_n \left(n \Delta \tau \right) \tag{2.2.10}$$

Root-mean-square and variance of a random variable

The mean of a random variable was defined in equations (2.2.7) – (2.2.10). One can use the variance of a random variable for characterizing the spreading. Alternatively, one can use the root of the variance, often referred to as the root-mean-square (rms) of the random variable instead. The rms is defined on the basis of the ensemble-average as follows:

$$\phi'_{rms} = \sqrt{\frac{1}{N} \sum_{n=1}^{N} \left(\phi_n - \langle \phi \rangle \right)^2} \tag{2.2.11}$$

Describing cycle-by-cycle variation

In piston engines, the mean flow and the mean thermodynamic quantities (e.g. in-cylinder pressure) can vary from cycle to cycle. This cycle-by-cycle variation (CCV) can be defined by use of an ensemble or phase average, since the ensemble-averaged mean is only a function of the crank angle since the cyclic variation has been averaged out [1]. Generally speaking, both an instantaneous flow and a thermodynamic quantity can be decomposed into three parts [1]: the component reflecting turbulence, the component reflecting cyclic variation, and the ensemble averaged mean. If there is a clear scale separation between the components due to cyclic variation and to turbulence, one can use time-averaging or space-averaging obtaining the statistics of turbulence that applies, after which the cyclic variation can be determined.

2.3 Governing Equations for Turbulent Reactive Flows in the Cylinder

The governing equations for in-cylinder flow and combustion can be derived based on the laws of mass conservation, momentum conservation and energy conservation. Since the present thesis deals with only gas mixtures, the source terms applying to phase change in the governing equations have been neglected.

During the compression and combustion strokes, the Mach number is typically low, e.g. $Ma < 0.3$. In such flows use can be made of the so-called low Mach number approximation, [75, 87]. With use of this approximation, the density in the cylinder can be found to change because variations in temperature but not because of spatial gradients in pressure. The physical pressure can be divided up into the thermodynamic and the hydrodynamic pressure. The thermodynamic pressure P is constant in space and only changes over time. It is used in equation of states to relate the gas density to the temperature providing a pressure in the order of 1 – 100 bars (10^5 – 10^7 Pa). The hydrodynamic pressure p is used in computing pressure gradients in the momentum equations in terms of which it is in the order of 1 – 100 Pa.

In the mathematical formulations of the governing equations, it is sometimes convenient to use the material derivation, which is defined as,

$$\frac{D\phi}{Dt} = \frac{\partial \phi}{\partial t} + \frac{\partial u_i \phi}{\partial x_j} \tag{2.3.1}$$

The governing equations discussed below are based on a Eulerian framework with use of a Cartesian coordinate, the three coordinates involved being denoted as x_i (i=1,2,3). The Einstein summation rule in three dimensions is used in the equations that follow.

Transport Equations of Mass and Species

On the basis of the Law of mass conservation, the continuity equation of a gas mixture can be written as follows:

$$\frac{\partial \rho}{\partial t} + \frac{\partial \rho u_i}{\partial x_i} = 0, \quad i = 1,2,3 \tag{2.3.2}$$

The governing equations for the species mass fraction can be derived on the basis of the Law of mass conservation for a multiple component gas mixture,

$$\frac{\partial \rho Y_n}{\partial t} + \frac{\partial \rho u_i Y_n}{\partial x_i} = \frac{\partial}{\partial x_i}\left(\rho D_n \frac{\partial Y_n}{\partial x_i}\right) + \omega_n, \quad n = 1,\ldots,N \tag{2.3.3}$$

where Y_n of species n in an N species mixture. D_n is the diffusion coefficient of species n and ω_n is the reaction rate of species n.

Transport Equation of Momentum

The momentum equations are derived from the Law of momentum conservation, the momentum equations there also being known as the Navier-Stokes equations.

$$\frac{\partial u_i}{\partial t} + \frac{\partial \rho u_i u_j}{\partial x_j} = -\frac{\partial p}{\partial x_i} + \frac{\partial \tau_{ij}}{\partial x_i}, \quad i = 1,2,3 \tag{2.3.4}$$

The last term on the right hand size represents the viscous tensor which can be written as

$$\tau_{ij} = \mu\left(\frac{\partial u_i}{\partial x_j} + \frac{\partial u_j}{\partial x_i}\right) - \frac{2}{3}\mu\delta_{ij}\frac{\partial u_k}{\partial x_k} \tag{2.3.5}$$

Transport Equation of Energy

The energy conservation equation based on enthalpy can be written as

$$\rho\frac{Dh}{Dt} - \frac{DP}{Dt} = \frac{\partial}{\partial x_j}\left[\rho\alpha\frac{\partial h_i}{\partial x_i} - \rho\alpha\sum_{n=1}^{N}\left(1 - \frac{1}{\mathrm{Le}_n}\right)h_n\frac{\partial Y_{ni}}{\partial x_i}\right] + \dot{Q}_r + \tau : \nabla\vec{\nu} \tag{2.3.6}$$

where the two last terms on the right hand side represent the radiative heat transfer and the viscous dissipation of energy, respectively. A low Mach number approximation indicates that, the viscous dissipation term in the energy equation can be neglected. The radiative heat transfer can also be neglected in the present study. Borman and Nishiwaki reviewed radiative heat transfer in IC engines [88]: They reported that radiative heat transfer in homogeneous charge combustion, in an SI engine for example is less important than it is in Diesel engines, due to the low soot level in SI engines. As a result, one can neglect the effect of radiative heat transfer on the combustion process in SI engines. In HCCI engines, the combustion temperature is generally low, due to the fuel-lean conditions aimed at avoiding the formation of NO_X. Thus in HCCI engines, the radiative heat transfer can be expected to be low.

The Lewis number, Le, is the ratio of the mass diffusion coefficient α, to the thermal diffusion coefficient D_n. In the thesis the Lewis number is set to unity, which corresponds to that the thermal and mass diffusivity being equal.

$$\mathrm{Le}_n \equiv \frac{\alpha}{D_n} = \frac{\lambda}{\rho C_p D_n} \tag{2.3.7}$$

According to the equation of state, the temperature, the species mass fraction and the density are all related to the thermodynamic pressure. The equation of state can be written as

$$P = \rho R_u T\sum_{n=1}^{N}\frac{Y_n}{W_n} \tag{2.3.8}$$

where R_u is the universal gas constant and W_n is the molecular weight of species n.

The calorific equation

The calorific equation is needed to compute the temperature of the gas mixture from the enthalpy and the mass fractions of the mixture.

$$h = Y_n h_n = Y_n\left(h_n^0 + \int_{T_{ref}}^{T} c_{p,n}dT\right) \tag{2.3.9}$$

where $c_{p,n}$ is the heat capacity of species n and h_n^0 is the enthalpy of formation under the standard reference condition, T_{ref} = 298K.

Chapter 3 Large Eddy Simulation of HCCI Combustion

The governing equations described in Chapter 2 are generally not possible to solve analytically due to the non-linearity of the system, or to solve numerically due to the existence of large spectra of turbulence eddies, which require such fine resolution in both space and time that even the fastest computers today cannot them handle within a reasonable length of time. A statistical average approach is generally introduced in connection with the governing equations, this leading to the small scales of turbulence and the reaction layers being averaged out. The effect of these small scales is taken into account in the governing equations for the averaged flow and thermodynamic quantities. This is the so-called modeling problem of turbulent combustion.

Several approaches to this date have been developed in the past, e.g. the Unsteady Reynolds Averaged Navier-Stokes equation approach, URANS, and the Large-Eddy Simulation, LES, approach. URANS has been widely used in connection with IC engine turbulence and in combustion simulations [29, 63, 71]. As discussed earlier, URANS is applicable when there is a distinct difference between the large-scale well-organized mean flow and the energy-containing turbulence eddies. The URANS approach averages out the energy-containing eddies in the governing equations; as such, the effect of the highly anisotropic energy-containing eddies need to be modeled. It is rather demanding to model such geometry-dependent highly anisotropic energetic eddies.

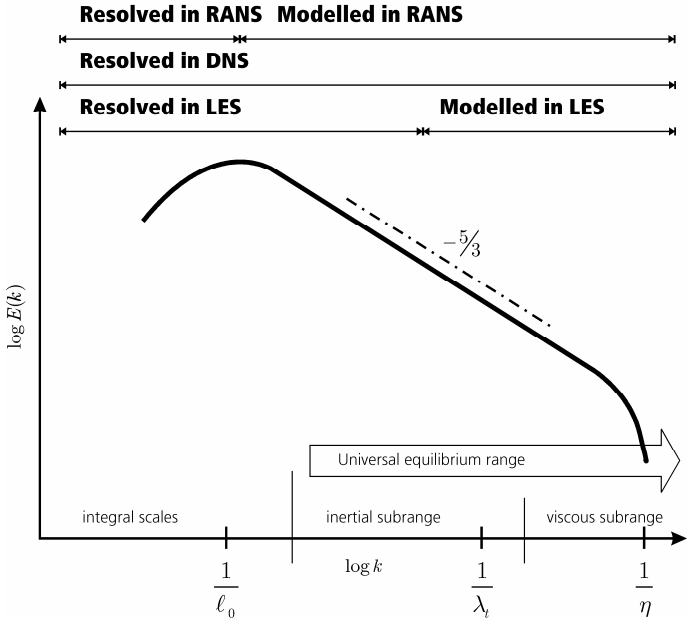

Figure 7: Model and resolved part of the Energy Spectrum for each of three methods; RANS, DNS and LES

Compared with URANS, the LES approach has the advantage of resolving both the mean flow and the large-scale energy-containing eddies of turbulence; the small-scale, local statistically isotropic turbulence eddies are modeled in the LES equations. The difficulty in modeling is less there, since the results are less sensitive to the effects of the small-scale eddies, these being filtered out in the LES equations.

Figure 7 shows schematically the resolved and modeled part of the energy spectrum of the different approaches to simulation available. When use is made of, URANS, the entire spectrum is modeled. In using LES the large energy-containing eddies and part of the inertial subrange of the spectrum are resolved, whereas the remaining part of inertial subrange and the entire viscous dissipation subrange are modeled. The most accurate method is Direct Numerical Simulation (DNS), which resolves the entire spectrum of turbulent kinetic energy, however, at a currently unaffordable computational cost when real engine geometry is involved.

The LES approach is employed in the present thesis, due to its high degree of accuracy and its reasonable computational costs. An introduction to engine LES is presented in this chapter, a presentation of the LES models for HCCI combustion and SACI combustions as developed in the thesis being included.

3.1 Reynolds and Favre Decomposition

In LES for turbulent reactive flows, two types of decomposition of the random variables are used most commonly: Reynolds- and Favre-decomposition respectively. In Reynolds-decomposition the instantaneous flow variables are decomposed into the filter-scale (FS) part $\overline{\phi}$ and the sub-filter-scale (SFS) part ϕ',

$$\phi = \overline{\phi} + \phi' \tag{3.1.1}$$

Since the filter-scale part is resolved in the LES grid, it is known as the resolved grid scale quantity; similarly the SFS part is also known as the sub-grid-scale (SGS) quantity. The overbar in equation (3.1.1) represents spatial filtering. Different filtering approaches can be used for LES; the top-hat filter or the Gaussian filter are typically used when finite-difference numerical methods are employed[89]; sharp Fourier cutoff filtering is implicitly used when Fourier spectral methods are used. The filter size is typically equal to or larger than the grid size employed in the numerical simulation. Assume that the spatial filter function has the following general form,

$$F(\psi_i) = F(\psi_i\{\Delta\}) \tag{3.1.2}$$

As an example, applying Reynolds filtering procedure to the density of the mixture,

$$\overline{\rho}(x_i,t;\Delta) = \int_{-\infty}^{\infty}\int_{-\infty}^{\infty}\int_{-\infty}^{\infty} F(x_i-\psi_i;\Delta)\rho(\psi_i,t)d\psi_i \tag{3.1.3}$$

yields a Reynolds filtered density. In flows having densities that vary in space, as in engines having fuel/air mixing or inhomogeneous reaction zones, density-weighted spatial-filtering, which is also known as Favre-filtering, is often employed. The spatial filtered continuity equation can be simplified by using Favre-averaging. The Favre-average is defined as,

$$\tilde{\phi} = \frac{\overline{\rho\phi}}{\overline{\rho}} \tag{3.1.4}$$

$$\phi = \tilde{\phi} + \phi'' \tag{3.1.5}$$

whereas Favre decomposition is defined as in equation (3.1.5). The over-tildes in these equations denote the Favre averaged (density-weighted spatial-filtered) quantities. The overbars are the same as in (3.1.1). One Favre-averaged quantity that of enthalpy, is determined as follows:

$$\tilde{h}(x_i,t;\Delta)=\frac{1}{\overline{\rho}}\int_{-\infty}^{\infty}\int_{-\infty}^{\infty}\int_{-\infty}^{\infty}F(x_i-\psi_i;\Delta)\rho(\psi_i,t)h(\psi_i,t)d\psi_i \tag{3.1.6}$$

3.2 Filtered Transport Equations

The governing transport equations for mass, momentum and energy can be written by use of Favre-filtering as follows: First the filtered continuity equation can be written as

$$\frac{\partial\overline{\rho}}{\partial t}+\frac{\partial\overline{\rho}\tilde{u}_i}{\partial x_i}=0 \tag{3.2.1}$$

The filtered species transport equation then can be written as

$$\frac{\partial\overline{\rho}\tilde{Y}_n}{\partial t}+\frac{\partial\overline{\rho}\tilde{u}_i\tilde{Y}_n}{\partial x_i}=\frac{\partial}{\partial x_i}\left(\overline{\rho}\overline{D}_n\frac{\partial\tilde{Y}_n}{\partial x_i}-\overline{\rho}\left(\widetilde{u_iY_n}-\tilde{u}_i\tilde{Y}_n\right)\right)+\overline{\omega}_n\,,\quad n=1,\ldots,N \tag{3.2.2}$$

The filtered transport equation for enthalpy, in turn, can be written as

$$\frac{\partial\overline{\rho}\tilde{h}}{\partial t}+\frac{\partial\overline{\rho}\tilde{h}\tilde{u}_j}{\partial x_j}=\frac{\partial\overline{p}}{\partial t}+\frac{\partial}{\partial x_j}\left(\overline{\rho}\alpha\frac{\partial\tilde{h}}{\partial x_j}\right)-\frac{\partial}{\partial x_j}\left[\overline{\rho}\left(\widetilde{hu_j}-\tilde{h}\tilde{u}_j\right)\right] \tag{3.2.3}$$

The filtered momentum equations, finally can be written as

$$\frac{\partial\overline{\rho}\tilde{u}_i}{\partial t}+\frac{\partial\overline{\rho}\tilde{u}_i\tilde{u}_j}{\partial x_j}=-\frac{\partial\overline{p}}{\partial x_i}+\frac{\partial}{\partial x_j}\left[\overline{\tau}_{ij}-\overline{\rho}\left(\widetilde{u_iu_j}-\tilde{u}_i\tilde{u}_j\right)\right] \tag{3.2.4}$$

In the filtered equations above, the SGS effect is taken into account by the following terms,

$$\widetilde{u_iY_n}-\tilde{u}_i\tilde{Y}_n\,,\quad\widetilde{hu_i}-\tilde{h}\tilde{u}_i\,,\quad\widetilde{u_iu_j}-\tilde{u}_i\tilde{u}_j \tag{3.2.5}$$

which represent respectively, the SGS transport flux of the species mass fractions, energy and momentum. The last term is also known as the SGS stress tensor,

$$\tau_{ij}^R=\widetilde{u_iu_j}-\tilde{u}_i\tilde{u}_j \tag{3.2.6}$$

It has already been indicated that in LES the main flow stream and the large-scale energy-containing part of the spectrum of turbulent kinetic energy are resolved. This resolved flow can be used to compute the statistics of the flow and of combustion. The role of SGS terms is not to provide these statistics directly, but to prevent omission of the unwanted scales from spoiling calculation of the scales from which the statistics aimed at are taken [89].

An important role of the SGS stress tensor is to provide a mechanism for energy transfer between the resolved scales. In the energy-cascade theory of homogeneous isotropic turbulence, energy is transferred from the large scales to small scale within the dissipation range the kinetic energy being dissipated to heat. The LES filter is typically in the inertial subrange, the energy being mainly transferred from the larger resolved grid scale to the smaller SGS. In some cases, however, such as near walls, the energy is transferred from smaller scales to large scales [89].

3.2.1 Smagorinsky and Scale Similarly models

The Smagorinsky model is a model commonly used for SGS transport fluxes [90]. It is also known as the eddy viscosity model, since it is always dissipative meaning that, can it deal with SGS in the role it plays in the energy transfer from large scale to smaller scales and with with energy dissipation within the viscous dissipation range of the spectrum. The Smagorinsky

model is similar to the Boussinesq hypothesis [83], used in the URANS approach (however, the two are based on completely different concepts):

$$\tau_{ij}^{R} - \frac{\delta_{ij}}{3}\tau_{ij}^{R} = -\nu_t\left(\frac{\partial \tilde{u}_i}{\partial x_j} + \frac{\partial \tilde{u}_j}{\partial x_i}\right) = -2\nu_t \tilde{S}_{ij} \tag{3.2.7}$$

where the ν_t is the SGS viscosity and $\tilde{S}_{ij}$ is the filtered rate of the strain tensor.

$$\tilde{S}_{ij} = \frac{1}{2}\left(\frac{\partial \tilde{u}_i}{\partial x_j} + \frac{\partial \tilde{u}_j}{\partial x_i}\right) \tag{3.2.8}$$

SGS viscosity can be modeled as

$$\nu_t = \left(C_s \Delta_{\mathrm{LES}}\right)^2 \left|\tilde{S}\right| \tag{3.2.9}$$

where Δ_{LES} is the filter size, which should be larger than the size of the simulation grid so as to ensure that the numerical grid can fully resolve the filter-scale quantities. $\left|\tilde{S}\right| = \sqrt{2\tilde{S}_{ij}\tilde{S}_{ij}}$ is the rate of strain on the resolved scale. C_{S} is a model constant, one which can be derived using DNS data or on the basis of theory. In many cases too, it can be tuned to be able to match the LES results to the experimental data. Several authors have reported the value of C_{S} to be 0.19 – 0.24 [91, 92]. In flows having shear, however, C_{S} needs to be reduced, e.g. 0.056 – 0.1 [93].

The main benefit of the Smagorinsky model is that it is simple to use and that it takes into account the role of energy dissipation at the SGS. Accordingly, it has become a basic model in many LES applications. The model suffers from several drawbacks, however. First, it is often too dissipative and the value of C_{S} is often found to be flow configuration dependent. Secondly, the SGS viscosity is always positive $\nu_t > 0$, so that the transfer of the energy only goes from the SGS to the resolved grid scales, i.e. backscattering [8]. A dynamic Smagorinsky model has been developed to circumvent these shortfalls, according to this model the constant C_{S} being determined dynamically through employing a test filter which is larger than the grid filter. Based on the Germano identity [94], the SGS stresses are related to the resolved turbulence stresses (Leonard stresses) and the subtest-scale stresses. Use of the Smagorinsky model to enable one approximate both the SGS stresses and the subtest-scale stresses contained in the Germano identity. Minimizing errors in this way makes it possible to determine the Smagorinsky constant dynamically as the computation proceeds. Details of the dynamic Smagorinsky model can be found in [94-96].

The Scale-Similarity Model (SSM) is another model that can take into account of energy backscattering. The basic assumption [97] made in connection with SSM is that the dominated parts of unresolved stresses are those close to the cutoff scale of the filter, and that the scales with which the SGS stresses interact most are just above the cutoff level. The model can be written as:

$$\tau_{ij}^{R} = \widetilde{\tilde{u}_i \tilde{u}_j} - \tilde{\tilde{u}}_i \tilde{\tilde{u}}_j \tag{3.2.10}$$

SSM has been found to not be dissipative enough [97]. A mixed model [97, 98], obtained by coupling SSM with Smagorinsky model was proposed to take into account of both the energy backscattering and the dissipation rate required.

$$\tau_{ij}^{R} = C_l\left(\widehat{\tilde{u}_i \tilde{u}_j} - \hat{\tilde{u}}_i \hat{\tilde{u}}_j\right) - 2\left(C_s \Delta_{\mathrm{LES}}\right)^2 \left|\tilde{S}\right| \tilde{S}_{ij} \tag{3.2.11}$$

where $\hat{}$ is a second filter and C_l is a model constant. SGS transport fluxes for the scalars, e.g. species mass fractions and the specific enthalpy, can be modeled using the Smagorinsky model. The Smagorinsky model can basically stabilize the numerical solution due to the model's dissipative nature. It is advantageous to apply the model to the scalar transport for example, since the wiggles in the numerical solution of the scalars can lead to nonphysical results (e.g. mass fractions less than zero or larger than 1, or temperatures less than 0 K), wiggles should be avoided.

3.3 Modeling of auto-ignition in HCCI combustion

Sub-models for auto-ignition front propagation involving a homogeneous charge but non-homogeneous temperature field have been developed for HCCI combustion (see [76, 99] and Paper 1). The model is based on a reaction progress variable proposed by Zhang et al. [100]. The reaction progress variable is the normalized cumulative heat release defined as

$$c = \frac{h(T_{ref}, Y_i) - h(T_{ref}, Y_{i,u})}{h(T_{ref}, Y_{i,b}) - h(T_{ref}, Y_{i,u})} \tag{3.3.1}$$

where

$h(T_{ref}, Y_i) =$ specific enthalpy of the charge defined at T_{ref}

$T_{ref} = 298\text{K}$ reference temperature

$Y_{i,u} =$ mass fractions of species contained in the unburned charge

$Y_{i,b} =$ mass fractions of species contained in the fully burned charge

It appears that

$$h(T_{ref} = 298K, Y_i) = \sum_{i=1}^{N} Y_i h_{i,f}^0 \tag{3.3.2}$$

where $h_{i,f}^0$ is the enthalpy of formation under standard (reference) condition. A transport equation for c can be derived from the conservation equations of mass and species mass fractions,

$$\frac{\partial \rho c}{\partial t} + \frac{\partial \rho u_j c}{\partial x_j} = \frac{\partial}{\partial x_j}\left(\rho D \frac{\partial c}{\partial x_j}\right) + \dot{\omega}_c \tag{3.3.3}$$

The source term $\dot{\omega}_c$ is obtained from tabulation of the auto-ignition history which applies (e.g. species mass fractions and temperature as a function of time) as a function of the reaction progress variable, enthalpy and thermodynamic pressure. The auto-ignition history is computed using detailed chemical kinetic mechanisms for the fuel in question.

In an LES context, subgrid effects on the source term need to be taken account of through use of a presumed PDF. When *c*, *h*, and *p* are known, the temperature of the charge at each grid point can be computed on the basis of auto-ignition tabulation,

$$T = f_1(h, p, c) \tag{3.3.4}$$

The thermodynamic pressure (in-cylinder pressure) is then determined from the gas temperature and from compositions based on global mass conservation and on the equation of state. The local density of the charge is determined from the equation of state.

3.4 Modeling of spark-assisted HCCI combustion

Spark-assisted compression ignition (SACI) is also known as spark-assisted HCCI or gasoline HCCI. Two modes are involved in the process: first, premixed flame propagation after spark-ignition of the charge and then following this, auto-ignition of the remaining charge. SI is to increase the in-cylinder temperature and pressure so that the large remaining volume of charge can be easily ignited.

Sub-models for the flame propagation and auto-ignition processes involved need to be developed to adapted for simulating SACI combustion. AI-front propagation described in the previous section is promising in this respect. Here, a description of premixed flame propagation is presented.

Models of several different types have been developed for PF propagation, such as the G-equation based level-set approach, reaction rate based progress variable approach, PDF based approaches and conditional moment closure approach. These approaches are interconnected since they model the same physical process. In the present work, the rate-based progress-variable approach to be consistent with the AI propagation model discussed above. This facilitates a consistent and easier implementation of the two models, and an easier formulation of models for hybrid modes. The same definition of the progress-variable *c* as in equation (3.3.1) is adopted, namely that for PF *c* also represents normalized cumulative heat release. The transport equation for *c*, equation (3.3.3) is derived from physical principles. In contrast to the AI model, the reaction rate for PF propagation in the LES context is modeled as follows [101, 102].

$$\dot{\omega}_c = \rho_u s_L \sum \tag{3.4.1}$$

where ρ_u is the density of the unburned charge, s_L is the laminar burning velocity of the charge; $\sum$ is the flame surface density. Transport equations for $\sum$ were used in (3.3.1)-(3.4.2). There are several unknown closure terms, however, that need to be modeled. Lack of such modeling increases the uncertainties present in the model. In the present work, is made of use a simplified model for $\sum$ which is derived below. First, it can be from equation (3.3.3) shown that

$$\int_{-\infty}^{+\infty} \dot{\omega}_c dx = [\![\rho v_n c]\!] + \int_{-\infty}^{+\infty} \frac{\partial \rho c}{\partial t} dx = [\![\rho v_n c]\!] \equiv \dot{m} \equiv \rho_u s_{sgs} \tag{3.4.2}$$

where $\dot{m}$ is the mass flux burned by the flame, and s_{sgs} is the burning velocity on the resolved LES scale. Since $\sum$ is likely to be high in the middle of the flame brush and small at the edge of the flame one can assume that

$$\sum = A(1-c)c \tag{3.4.3}$$

where A is a proportionality constant to be determined. From equations (3.4.1),(3.4.2) ,(3.4.3) it appears that

$$\rho_u s_{sgs} = \int_{-\infty}^{+\infty} \dot{\omega}_c dx = \rho_u s_L \int_{-\infty}^{+\infty} \sum dx = \rho_u s_L A \int_{-\infty}^{+\infty} (1-c)c dx = \rho_u s_L A g \tag{3.4.4}$$

Thus,

$$Ag = s_{sgs} / s_L = 1 + u' \tag{3.4.5}$$

where g is the integral to be discussed below. From (3.4.1)-(3.4.5) one has

$$\begin{aligned}\dot{\omega}_c &= \rho_u s_L \sum = \rho_u s_L A(1-c)c = \rho_u s_{sgs} g^{-1}(1-c)c \\ &= \rho_u s_L g^{-1}(1+u')(1-c)c \\ &= \rho_u s_L (1+u')(1-c)c\left(\int_{-\infty}^{+\infty}(1-c)cdx\right)^{-1}\end{aligned} \tag{3.4.6}$$

g can be estimated (and modeled) as follows

$$g = \int_{-\infty}^{+\infty}(1-c)cdx \simeq \left(\frac{dc}{dx}\right)^{-1}\int_0^1(1-c)cdc = \left(\frac{dc}{dx}\right)^{-1}/6 \simeq \alpha\Delta/6 \tag{3.4.7}$$

Δ is the LES filter size. In the equation above the mean gradient of the reaction progress variable has been estimated as $1/\alpha\Delta$, its being assumed there that the filtered reaction zone has a thickness of $\alpha\Delta$. The model parameter α represents the ratio of the thickness of the filtered reaction zone to the filter size. In the present study, the filter size was set to be the grid size, and α was set to 6, which implies that the reaction zone is filtered to within 6 grid cells. This has been found to be helpful for the stability of the numerical solver. From (3.4.6) and (3.4.7), one can derive

$$\dot{\omega}_c = \frac{6\rho_u s_L(1+u')(1-c)c}{\alpha\Delta} \tag{3.4.8}$$

In this model, ρ_u and s_L are needed. They can be determined from thermodynamic relationships as follows [1]:

$$s_L = s_L^o\left(\frac{T_u}{T_0}\right)^{\alpha}\left(\frac{p}{p_0}\right)^{\beta} \tag{3.4.9}$$

where the subscript 0 denotes the standard conditions under which the flame speed s_L^0 was determined. The constants in the model are as follows

$$\begin{aligned}\alpha &= 2.18 - 0.8(\phi-1) \\ \beta &= -0.16 + 0.22(\phi-1)\end{aligned} \tag{3.4.10}$$

where $\phi = 1/\lambda$ is the fuel equivalence ratio. In equations (3.4.8) and (3.4.9) one needs to determine ρ_u and T_u, which are the density and the temperature of the charge at unburned conditions. These can be determined from the local density and the temperature as follows. Assume that the molar number does not change markedly during combustion. This is the case for stoichiometric or lean combustion. From equation of state one then has

$$\begin{aligned}\rho_u &= \rho T / T_u \\ T_u &= f_1(p, h, c=0)\end{aligned} \tag{3.4.11}$$

Once *c* is computed, one can use the AI library to determine the local species, the temperature and then the pressure as well as the density. This model is a good one, although strictly speaking one needs to have a different set of libraries for the premixed flames.

The PF propagation model will be used for the PF front, generally whereas in places far from the PF front, use will be made of the AI model. These two models can be generalized as follows,

$$\dot{\omega}_c = \max(\dot{\omega}_{c,AI}, \dot{\omega}_{c,PF}) \tag{3.4.12}$$

In places where HCCI ignition is important the rate obtained from the HCCI model will be higher than that for premixed flame propagation. In places where the temperature is too low for auto-ignition to take place, the rate obtained from the HCCI model will be low and a premixed flame will be dominant. In places where it is possible to have both HCCI and a premixed flame, the dominant modes will have higher rates.

Alternatively, one can employ two progress variables (and thus two transport equations that apply to these progress-variables) to couple the SI flame with HCCI ignition; one of the two progress variable is for tracking the SI flame propagation, and the other one applies to the HCCI ignition process. The coupling of the two is more straightforward: at a given spatial location in the cylinder, when the progress variable for the SI flame is higher than that for the HCCI ignition, it is assumed that the SI flame prevails in the location in question. Thus, one can use the maximum of the two progress variables for determining the thermodynamic variables. This approach is used in the present study.

3.5 Boundary conditions

3.5.1 Wall models

A major difficulty in connection with the LES of in-cylinder turbulence and heat-transfer is the handling of the wall boundary layer. This difficulty arises because of the turbulence generation in the wall shear-layer being on a very fine scale, which is difficult to resolve. If the scale is filtered out to SGS, care must be taken in modeling the effect of the SGS eddies involved. The wall model is also a challenge in LES, and in practice one adopts different approaches, such as that of a ''wall-function'' that models the heat flux at the wall by using flow quantities from the first cell near the wall,

$$\overline{\rho} D \left.\frac{\partial \tilde{h}}{\partial y}\right|_{wall} / \tau_{wall} \simeq \left(\frac{1}{\mathrm{Pr}} \frac{\partial \tilde{h}}{\partial y} / \frac{\partial \tilde{u}}{\partial y}\right)_{\text{first grid}} \simeq \left(\frac{1}{\mathrm{Pr}} \frac{\partial \tilde{h}}{\partial \tilde{u}}\right)_{\text{first grid}} \tag{3.5.1}$$

where y is the local direction normal to the wall and τ is the wall shear stress; the subscript "first grid" denotes the first grid point next to the wall. The Prandtl number is typically set to 0.7. This approach has been used in [103, 104]. A comprehensive survey of wall models for LES, in which alternative models are also taken up can be found in [105]. Prandtl number is defined as

$$\mathrm{Pr} = \frac{\nu}{\alpha} \tag{3.5.2}$$

One should note that in the wall boundary layer the general spatial filtering approach is no longer valid, since the theoretical basis, the energy spectrum of turbulence kinetic energy as shown in figure 7, does not hold in the near wall region. Some authors use RANS models to compute the flow in the wall boundary layer and LES for the outer flow, coupling the results obtained at the outer boundary of the wall boundary layer. Doing so results in the so-called Detached Eddy Simulation (DES). Hasse et al. [106-108] used the DES approach for simulating tumble flow motion and cyclic variation in IC engines and vortex shedding past a bluff-body flame holder [106-108]. They showed that DES could successfully capture the major statistics of flow here, including the cyclic variations applying to the processing core of the tumble vortex.

3.5.2 Inlet manifolds

The inlet manifolds flow has a large impact on the turbulence formation of the in-cylinder gas. To generate large-scale flows of these types as described in Section 2.1, and to keep the computational costs low, the valves geometry need to be taken into account on the basis of the inflow boundary conditions in the cylinder. The intake manifolds can be modeled as annular jets, where the solid center block represents the valve.

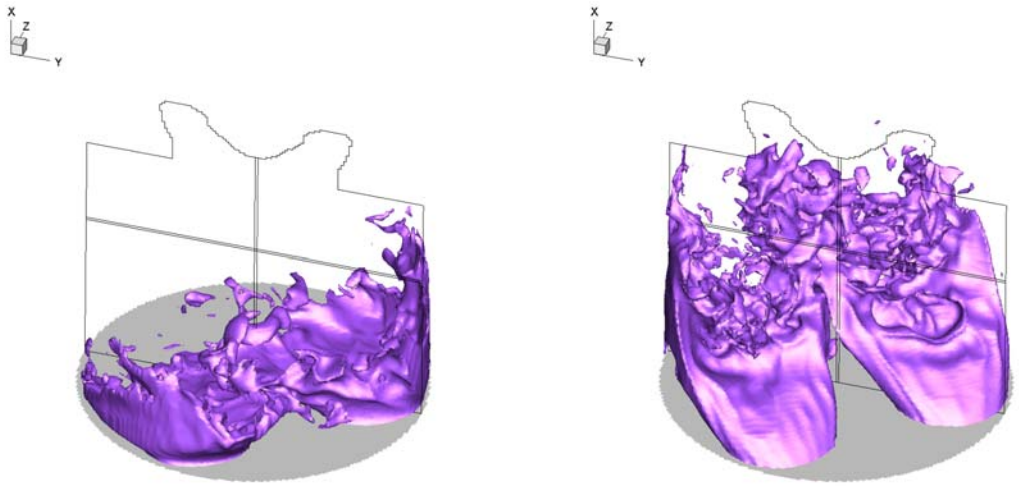

Figure 8: Three-dimensional instantaneous flow field at 90 CAD, from Paper 5, showing the inlet manifold difference between including and excluding inlet-swirl motion. Iso-contours showing the temperature at 355 K. The cylinder at the left has an inlet-swirl number. The cylinder at the right has a straight inlet flow trajectory.

The swirl flow can be also taken into account by specifying the axial and radial momentum components of the flow [109]. Figure 8 presents two examples of the flow structures near the intake manifolds. Further discussion of the inflow boundary conditions that are modeled can be found in references [38, 103].

Chapter 4 Numerical Methods of LES on HCCI combustion

The governing equations discussed in Chapter 3 are solved here using a high-order finite-difference approach on a staggered deforming Cartesian grid. A brief description of the method is presented here. A more detailed account is provided in [38].

4.1 The grid system

So as to be able to achieve both a higher order discretization and a high degree of computational efficiency use was made of a staggered Cartesian grid that had deforming coordinates. In a staggered grid, the scalar variables, involved such as in the present case, density ρ, hydrodynamic pressure p, enthalpy h and the progress variable c, are defined in the cell center. The three velocity components here, (u, v, w), are defined on the cell surface. Cartesian grids have the drawback that it is complex to describe the wall and piston geometries, the inlet manifolds and the valves in question. To overcome this drawback a use is made of boundary-correction algorithm [110] here in which the wall geometry and wall boundary conditions were taken into account by use of a high-order interpolation method. The moving piston is accommodated by use of the deforming coordinates (ξ, y, z). The governing equations described in the previous chapter had to be transformed here to the deforming coordinate system [38].

4.2 Spatial Discretization

The convective terms in the governing equations are discretizated using a 5th order Weighted Essentially Non-Oscillatory (WENO) scheme. The diffusive terms are discretized using a 4th order, central difference scheme [111]. The WENO scheme avoids numerical oscillations in the solutions. In scalar transport numerical oscillations, such as wiggles in the solutions, can lead to non-physical solution (such as involving a mass fraction of less than zero). With use of the WENO scheme, the SSM model for the SGS stresses, employed without use of the Smagorinsky model, is shown to give satisfactory degree of numerical stability as well as satisfactory energy transfer at the cutoff scales of the filter.

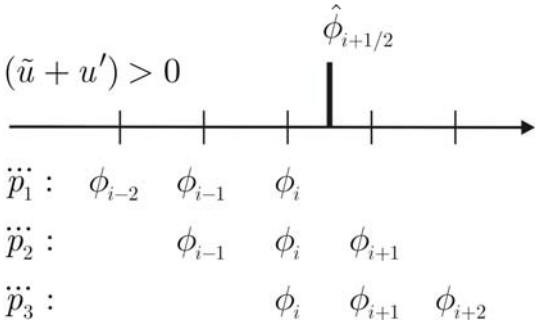

Figure 9: Candidate stencils for the 5th order WENO scheme (its being assumed that local convection is pointing to the right)

The WENO scheme is an adaptive stencil method, based on the idea of estimating first derivatives with use of several candidate stencils [112, 113]. The 5th order WENO scheme with use of in the thesis can then be written as [114, 115],

$$\left(\frac{\partial \phi}{\partial x}\right)_i = \frac{\hat{\phi}_{i+1/2} - \hat{\phi}_{i-1/2}}{\Delta x}$$
$$\hat{\phi}_{i+1/2} = \ddot{p}(x)\big|_{i+1/2} - \frac{\Delta x^2}{24}\left(\frac{\partial^2 \ddot{p}(x)}{\partial x^2}\right)_{i+1/2} \tag{4.2.1}$$

where $\ddot{p}(x)$ is a three-point polynomial interpolant to ϕ. Figure 9 illustrates the stencils used for the interpolants given that the convection velocity is positive $(\tilde{u} + u') > 0$. Three points, $\ddot{p}_1(x) : (\phi_{i-2}, \phi_{i-1}, \phi_i)$, $\ddot{p}_2(x) : (\phi_{i-1}, \phi_i, \phi_{i+1})$, and $\ddot{p}_3(x) : (\phi_i, \phi_{i+1}, \phi_{i+2})$, are selected around ϕ_i for constructing $\ddot{p}(x)$. The values of $\hat{\phi}_{i+1/2}$ can be computed by combining the following three polynomials:

$$\hat{\phi}^{(1)}_{i+1/2} = \frac{1}{3}\phi_{i-2} - \frac{7}{6}\phi_{i-1} + \frac{11}{6}\phi_i$$
$$\hat{\phi}^{(2)}_{i+1/2} = -\frac{1}{6}\phi_{i-1} + \frac{5}{6}\phi_i + \frac{1}{3}\phi_{i+1}$$
$$\hat{\phi}^{(3)}_{i+1/2} = \frac{1}{3}\phi_i - \frac{5}{6}\phi_{i+1} + \frac{1}{6}\phi_{i+2}$$

With a linear combination of the above values, finally, $\hat{\phi}_{i+1/2}$ can be evaluated as

$$\hat{\phi}_{i+1/2} = \omega_1 \hat{\phi}^{(1)}_{i+1/2} + \omega_2 \hat{\phi}^{(2)}_{i+1/2} + \omega_3 \hat{\phi}^{(3)}_{i+1/2}$$

where

$$\omega_k = \frac{\alpha_k}{\alpha_1 + \alpha_2 + \alpha_3}, \quad \alpha_k = \frac{\zeta_k}{\varepsilon + \beta_k}, \quad k = 1,2,3$$

ε is a small number, e.g. $\varepsilon = 10^{-6}$, added to the denominator to avoid its becoming zero. ζ_k are optimal weights, which are $\zeta_1 = 0.1$, $\zeta_2 = 0.6$, $\zeta_3 = 0.3$ respectively,

$$\beta_1 = \frac{13}{12}\left(\phi_{i-2} - 2\phi_{i-1} + \phi_i\right)^2 + \frac{1}{4}\left(\phi_{i-2} - 4\phi_{i-1} + 3\phi_i\right)^2$$
$$\beta_2 = \frac{13}{12}\left(\phi_{i-1} - 2\phi_i + \phi_{i+1}\right)^2 + \frac{1}{4}\left(\phi_{i-1} - 4\phi_{i+1}\right)^2$$
$$\beta_3 = \frac{13}{12}\left(\phi_i - 2\phi_{i+1} + \phi_{i+2}\right)^2 + \frac{1}{4}\left(3\phi_i - 4\phi_{i+1} + \phi_{i+2}\right)^2$$

The accuracy, efficiency and resolution properties of the 5th order WENO scheme in comparison were schemes have been demonstrated in [116].

The diffusion terms were computed using a 4th order central difference scheme [110, 117-119],

$$\left(\frac{\partial^2 \phi}{\partial x^2}\right)_i \approx \frac{-\phi_{i+2} + 16\phi_{i+1} - 30\phi_i + 16\phi_{i-1} - \phi_{i-2}}{12\left(\Delta x\right)^2} \tag{4.2.2}$$

4.3 Temporal Integration

In an engine cylinder the density of the gas mixture changes in space due to temperature stratification, composition stratification and reaction front propagation. In the case of existence of a reaction front, whether an SI flame-front or an HCCI ignition-front, the density gradients can be rather high. Earlier studies have shown [117, 120] that conventional

fraction-step methods suffer from numerical instabilities when the density ratio of the unburned to the burned gas is larger than 3 [121, 122].

The Predictor-Corrector method is an approach aimed at enhancing the numerical stability for density ratios of moderate size (less than 7) [123-125]. The method involves use of the continuity equation of the form $-\partial \rho u_i / \partial x_i = \partial \rho / \partial t$. In the predictor-step, user is made of the conventional fractional-step method [120]. A corrector-step is then employed to enhance the numerical stability.

In the thesis use is made of, a 2nd order Adam–Bashforth method in the predictor-step and a 2nd order Crank–Nicolson method in the corrector-step. For example, for a one dimensional scalar transport equation,

$$\frac{\partial \phi}{\partial t} = \frac{\partial \phi}{\partial x} + \frac{\partial^2 \phi}{\partial x^2} \tag{4.3.1}$$

the 2nd order Adam – Bashforth predictor method can be written as

$$\phi_i^{n+1} = \phi_i^n + \frac{\Delta t}{2}\left[3\left(\frac{\phi_{i+1}^n - \phi_{i-1}^n}{2\,\Delta x} + \frac{\phi_{i+1}^n - 2\phi_i^n + \phi_{i-1}^n}{(\Delta x)^2} \right) - \left(\frac{\phi_{i+1}^{n-1} - \phi_{i-1}^{n-1}}{2\,\Delta x} + \frac{\phi_{i+1}^{n-1} - 2\phi_i^{n-1} + \phi_{i-1}^{n-1}}{(\Delta x)^2} \right) \right] \tag{4.3.2}$$

and the 2nd order Crank-Nicolson method, used then for the corrector step is

$$\phi_i^{n+1} = \phi_i^n + \frac{\Delta t}{2}\left[\frac{\phi_{i+1}^{n+1} - \phi_{i-1}^{n+1}}{2\,\Delta x} + \frac{\phi_{i+1}^{n+1} - 2\phi_i^{n+1} + \phi_{i-1}^{n+1}}{(\Delta x)^2} \right] + \frac{\Delta t}{2}\left[\frac{\phi_{i+1}^{n} - \phi_{i-1}^{n}}{2\,\Delta x} + \frac{\phi_{i+1}^{n} - 2\phi_i^{n} + \phi_{i-1}^{n}}{(\Delta x)^2} \right] \tag{4.3.3}$$

To gain computational efficiency, the corrector-step is employed only when high density gradients can appear such as close to TDC.

4.4 Solution Methods

The discretized system of governing equations employs non-linear algebraic equations at a given time step. The system of algebraic equations is solved in the following steps [38].

The Predictor Step Calculations

Step 1 Calculation of in-cylinder thermodynamic pressure

Monitoring all the valves that are opened, enables the new in-cylinder total mass can be computed. The thermodynamic pressure can then be updated using the equation of state.

Step 2 Transport equations of enthalpy and progress variable c

In this step the discretized equations for enthalpy and progress variable are computed using the Adam-Bashforth time-stepping (4.3.2). At the end of this step the density field can be updated.

Step 3 Continuity equation and momentum equations

The density time derivative term in the continuity equation can then be estimated with use of the updated density field. Except for the hydrodynamic pressure gradient term, the momentum equations are used to advance the velocity field using Adam-Bashforth time stepping. The hydrodynamic pressure is then calculated by solving a Poisson equation numerically. The pressure gradient is then added to complete calculation of velocity in the predictor step. At the end of the predictor step, if no corrector step is required all the variables will already be at the new time step.

The Corrector Step Calculations

Step 4 Transport equation of enthalpy and progress variable

To enhance the numerical stability in case large density ratios are obtained, a modified Crank-Nicolson (4.3.3) time-stepping computation is performed, using the enthalpy and the progress variable equations. The modified Crank-Nicolson method is explicit about using the value calculated in the predictor-step to replace the value at the new time step (t^{n+1}). At the end of this step, the density field can also be updated.

Step 5 Poisson equations on pressure

Just as in the predictor-step, the new density value is used to determine a Poisson equation for the new hydrodynamic pressure. The velocity is also corrected so as to take account of the updated pressure gradient term.

Chapter 5 Results and Discussions

In this chapter, a brief summary of the main results obtained in this thesis is presented. The thesis work can be divided up into four categories as listed below,

- Investigation of the reaction front structures in HCCI combustion, investigating the effect of cylinder geometry, turbulence and temperature stratification on the HCCI combustion process; the main results are presented in Papers 1 and 2.
- Investigation of the development of turbulence and temperature stratification in HCCI engines; the main results are presented in Papers 1, 2, 3, 4, and 6.
- Investigation of composition stratification in HCCI engines having negative valve overlap and its effect on ignition; the correlations found between composition stratification and temperature stratification, and the sensitivity of ignition to composition stratification are investigated; the results are presented in Paper 3.
- Investigation of SACI combustion, focusing on the interaction of SI flame propagation and HCCI ignition and the effects of turbulence and the initial temperature field on SACI combustion; the results are summarized in Paper 5.

Port-fuel injection (PFI) was used in all the studies dealt within the thesis, modeling of the processes involved in liquid fuel injection and in evaporation thus being excluded. The fuel involved was limited to ethanol so as to compare the results with those of engine experiments in which ethanol was used exclusively.

5.1 Effect of Combustor Geometry on HCCI combustion

Since the experimental work of Christensen, Hultqvist and Johansson [15, 26] on the effect of combustor geometry on HCCI engines was carried out, several experimental investigations have been conducted with the aim of obtaining a better understanding of the effects of cylinder and piston geometry on the HCCI combustion process. Vressner et al. [73, 74] developed an optical HCCI engine based on a heavy-duty Scania D12 engine. The engine had a stroke of 154 mm, a bore of 127 mm, a connecting rod of 255 mm, and the compression ratio of 17:1. Three piston configurations were considered. The baseline reference piston engine had a metal square-bowl piston (referred to hereafter as MSB). The bowl, having equal sides 47 mm in length, and a depth of 37.4 mm, is located in the center of the piston. The other two piston engines are optically accessible, the one having a quartz liner and a quartz piston, having a flat disc shape (QD) and the other having the square-bowl-in-piston geometry (QSB) (the same bowl geometry as MSB). The pancake shaped and square bowls are shown in figure 10. For further details regarding the engine configurations see [73, 74].

In the experiments, the fuel employed is a mixture of ethanol and acetone, its having a concentration ratio of 9/1 and a specific air/fuel ratio of 3.3. The engine speed is 1200 rpm. The in-cylinder pressure is recorded in the center of the combustion chamber top using a piezoelectric water-cooled Kistler 7061B pressure transducer. The information obtained is used to control the combustion phasing by changing the inlet air temperature by use of an electrical heater. In all the experiments, the timing of 50 % heat release is kept at 8 crank angle degrees (CAD) after top-dead-center (TDC). The temperatures of the intake gas are 388 K, 400 K, and 354 K, for MSB, QD, and QSB, respectively.

A high-speed camera is used to record chemiluminescence images. The camera, a Phantom v7.1 from Vision Research, has a temporal resolution of 21.6 kHz, which corresponds to 3 CAD at 1200 rpm. PLIF of the fuel-tracer acetone focusing in the center of the combustion chamber is performed using a Multi:YAG laser cluster [75]. In the QSB engine, the laser sheet is positioned half-way up from the bottom of the bowl. Time separation between the PLIF images is 70 μs or 140 μs, which provides 1 or 2 images per CAD at the present engine speed.

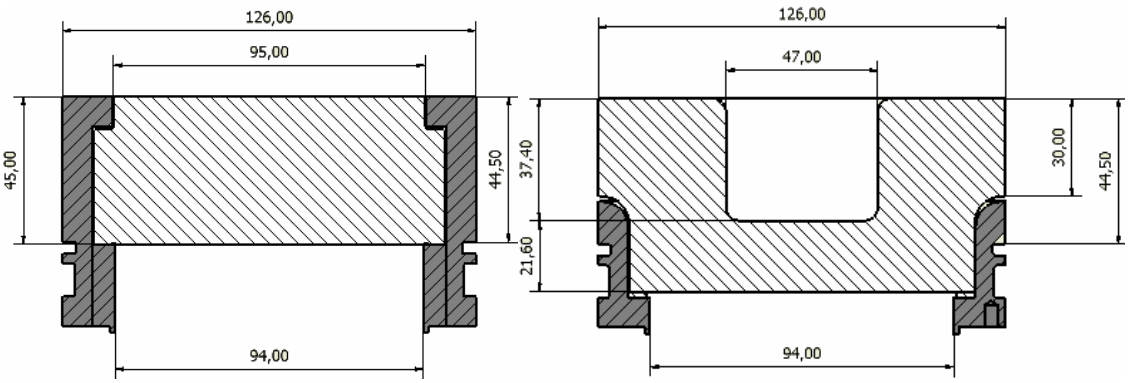

Figure 10: Cross section of the disc piston (left) and cross section of the square bowl piston (right). The white lined area indicates the parts that are quartz and the gray lined areas the parts that are titanium. Dimensions shown are in mm [73].

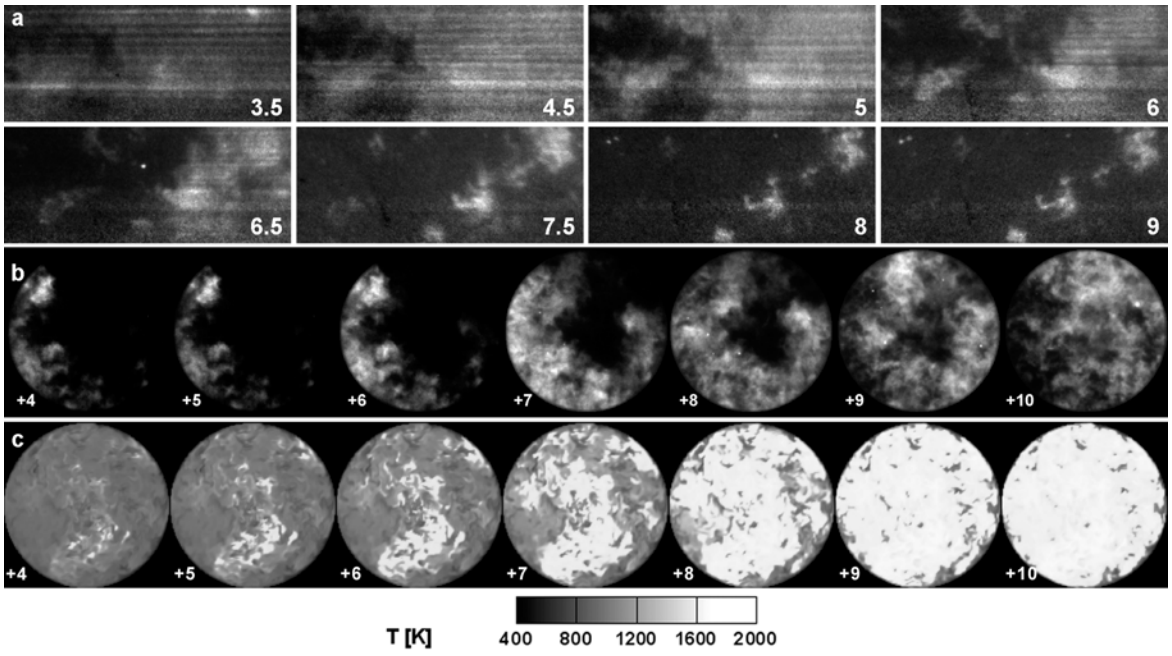

Figure 11: Sequences of instantaneous fields in the engine, the flat disc piston showing the development of the ignition process. (a) Fuel (acetone) LIF images (while: high acetone concentration, black/dark: low acetone concentration); (b) chemiluminescence imaging (white: combusted high-temperature zone; dark/black: low-temperature unburned region); (c) LES instantaneous temperature field (cf. temperature legend). The acetone LIF has an image window of 30 mm × 67 mm in the center of the bore; the LES results are shown in the same cut plane as the acetone LIF image. The lambda is 3.3. The 50% heat release was controlled at the crank angle 8 degrees after TDC.

Figure 11a shows eight PLIF images taken in one engine cycle for the QD case obtained with use of the Multi:YAG laser. The PLIF images show an area of 30 mm × 67 mm around the center of the cylinder. The darker areas indicate zones containing burned gas and the brighter areas indicate the as yet unburned parts. Since acetone is rapidly consumed at high temperature together with the main fuel consumption, it is appropriate to correlate the consumption of acetone with the consumption of the main fuel [62]. The fuel PLIF images show the ignition kernels which are distributed rather inhomogeneously.

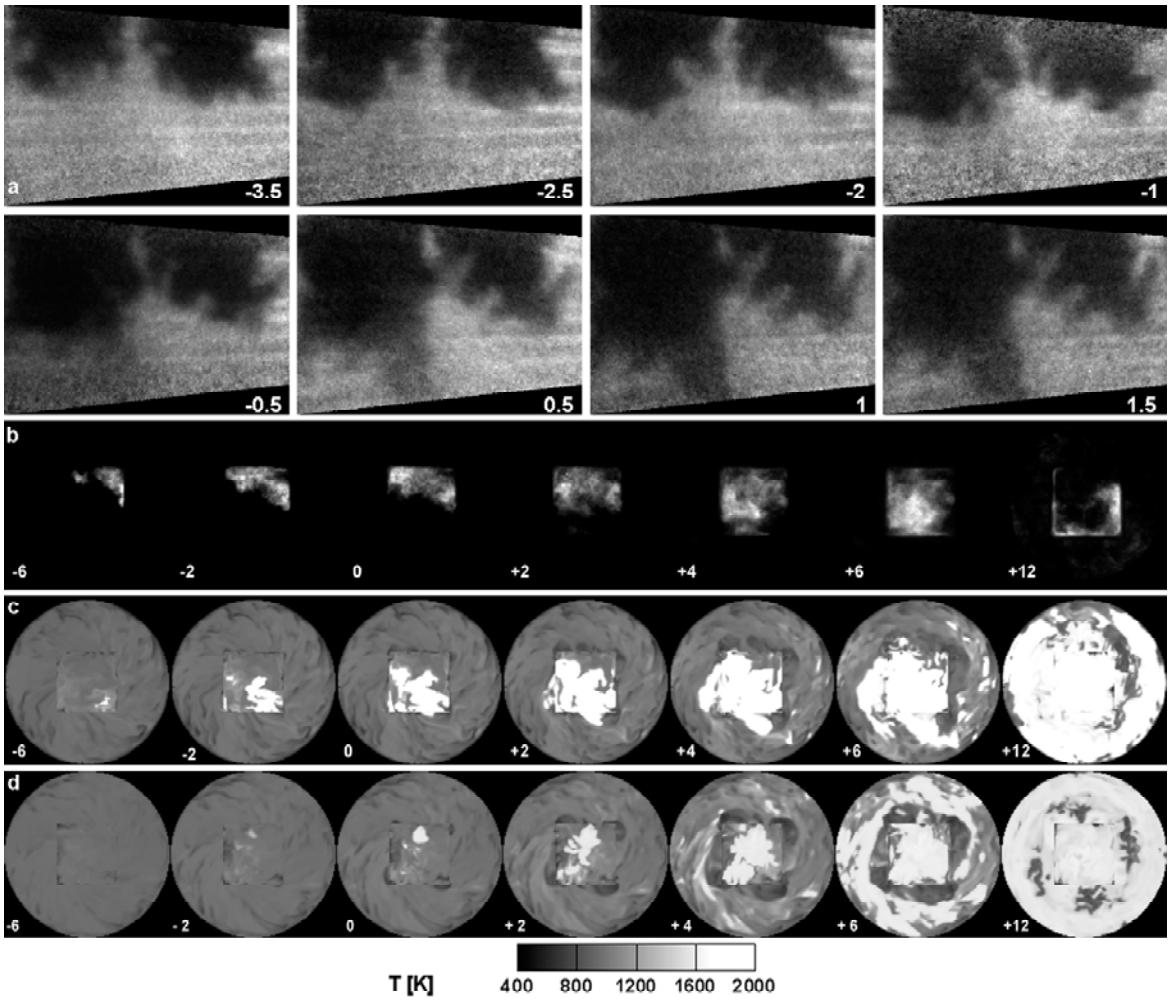

Figure 12: Sequences of instantaneous fields in the square-bowl engines showing the development of the ignition process. (a) Fuel (acetone) LIF images in the QSB engine (while: high acetone concentration, black/dark: low acetone concentration); (b) chemiluminescence imaging in the QSB engine (white: combusted high-temperature zone; dark/black: low-temperature unburned region); (c) LES instantaneous temperature field (cf. temperature legend) in the QSB engine; (d) LES instantaneous temperature field (cf. temperature legend) in the MSB engine. In (a) the acetone LIF show an image window of 30 mm × 45 mm in the center of the bore; in (c,d) images of two cut-planes are superimposed together: one cut is in the middle of the bowl and the other is in the middle of the squish room. The lambda is 3.3. The 50% heat release was controlled at the crank angle 8 degrees after TDC.

The corresponding images of acetone PLIF and of chemiluminescence for the QSB engine are shown in figure 12. Because of the strong focusing effect on the laser sheet from the quartz piston bowl the laser sheet was convergent in the combustion chamber. The image area is 30 mm × 45 mm. Figure 12a shows rather sharp, finger-like ignition kernel fronts in the center bowl region. These grow in a way similar to a 'premixed flame front', consistent with the DNS of lean H_2/air combustion in a constant volume vessel [69].

By comparing figure 11b with figure 12b, one can note that ignition starts much earlier in the QSB than in the QD case in which the combustion phasing in terms of 50 % heat release occurs at the same CAD. The chemiluminescence intensity in figure 12b appears first in the upper right corner of the bowl at –6 CAD. The boundary between the burnt and unburned zone is sharper suggesting there to be a steeper stratification in temperature. After TDC, the

chemiluminescence intensity increases in the QSB case, appearing first along the walls of the bowl and finally in the squish volume. At 12 CAD the combusted zone in the bowl becomes dark and the combustion front has spread to the squish zone. The signal disappears completely after 20 CAD, suggesting longer combustion duration than for QD.

Figure 13 shows the in-cylinder pressure from the measurements. As can be seen, the QSB engine has the slowest pressure-rise-rate, whereas the QD and the MSB engines have higher pressure-rise-rates of around 10 CAD after TDC. The in-cylinder pressure in the QD and the QSB engines correspond closely to the PLIF images and chemiluminescence images discussed earlier. The results for the MSB engine are surprising, there are being more similar to the results for the QD engine than to those for the QSB engines, although the QSB and MSB engines are very similar in terms of their combustor geometry.

Several hypotheses can be made to explain the experimental results obtained. The differences observed in the combustion behavior in the three engines are due to (a) the differences in the turbulence fields of the cylinders; (b) the differences in the temperature fields of the cylinders; (c) the differences in the mixing process of fuel/air and the residual gas in the cylinders.

To investigate these hypotheses, LES was carried out for the HCCI model discussed in Chapter 3. First, the detailed ethanol/air chemical kinetic mechanism [126] was used to simulate the auto-ignition process of the mixture of different initial temperatures and pressures. The auto-ignition history (i.e. the evolution of all the species mass fractions, temperatures, etc.) was tabulated as a function of the initial specific enthalpy, the pressure and the reaction progress variable at an air/fuel ratio of 3.3.

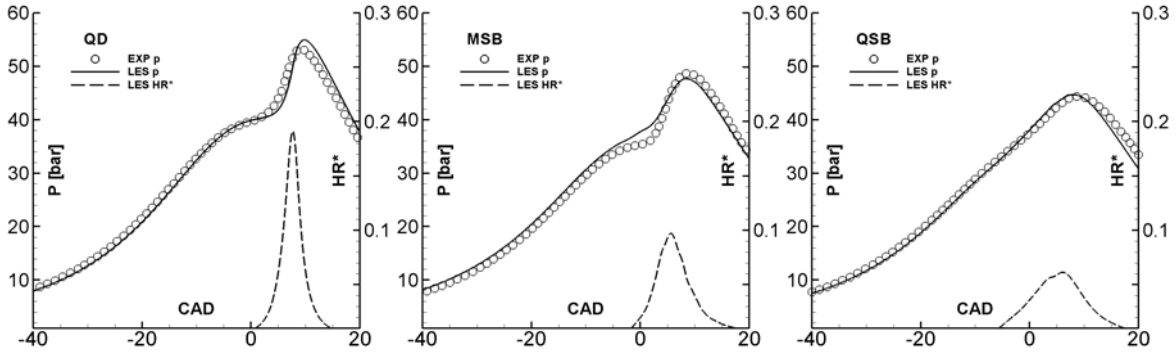

Figure 13: In-cylinder pressure in the experimental engines containing three different pistons. (a) QD engine, (b) MSB engine, (c) QSB engine.

The inflow conditions of LES such as the inlet gas temperature, the pressure and the mass flow rates were taken from the experiments. The two intake valves were modeled as annular jets [103]. Non-slip conditions and wall-functions [38] were used on the walls. The wall temperature of the water-cooled metal cylinder was estimated to be 510 K and that of the quartz piston to be 610 K, both of these being air-cooled to provide optical access. The initial flow conditions were set at –360 CAD, the residual gas temperature there being assumed to be 500 K. A value of –360 CAD was the TDC for the intake stroke. The flow and gas-temperature distribution, close to 0 CAD prior TDC, were not found to be affected by the previous cycle, since the trapped residual gas represents only about 5 % of the total mass in the cylinder during the combustion stroke.

A grid consisting of $128 \times 128 \times 128$ mesh cells was employed. The mesh had a size in the radial direction of about 1 mm, whereas in the axial direction it varied between 0.32 mm at TDC and 1.5 mm at BDC (bottom-dead-center) in the cases involving the square bowl, and between 0.075 mm at TDC and 1.3 mm at BDC in the case of QD. This mesh size is in the order of the Taylor micro-scales. Eight parallel processors were used in LES. This provides a simulation of a single cycle within 48 hours.

Figure 11c shows the instantaneous temperature distribution at the middle plane of the cylinder volume at different CAD within a given engine cycle, obtained using LES. The white zone represents temperatures higher than 1600 K. The ignition process simulated by LES is qualitatively similar to what is shown in the PLIF and chemiluminescence images. The inhomogeneity in temperature developed during the intake and compression strokes. Mixtures with higher temperature tend to ignite first. These ignition kernels propagate to the regions surrounding them. The ignition kernels grow and propagate in a counter-clockwise direction, the same direction as the swirling stream of the in-cylinder flow. At 7 CAD and thereafter, propagation becomes very rapid, similar to that shown in the chemiluminescence and PLIF images.

Figures 12c and 12d show the LES temperature fields in the QSB and MSB engines, respectively. To visualize the bowl zone and the squish at the same time, the two planes overlap the one intersecting the middle plane of the bowl and the other intersecting the middle plane of the squish volume. Due to the high temperature that develops in the region of the bowl prior to auto-ignition, the onset of auto-ignition is earlier in the bowl. The heat in the combusting zone in the bowl is transported rapidly due to the high temperature gradient between the burned and the unburned zones, its igniting the adjacent mixture in the bowl. The finger-like front there is formed through the strong flow and heat transport in the bowl, which can be seen in the PLIF images.

The LES results also indicate that after 4 CAD has been reached, the combustion front in the QSB engine advances in the direction of the squish volume. The large-scale swirl-flow motion can be clearly see in these temperature fields. The LES temperature field of MSB (which has the same geometry as that of QSB although the wall material is metal instead). Combustion in the metal engine is initiated in the bowl as well, the ignition fronts propagating counter-clockwise, following the swirl-flow stream direction. When combustion phasing in the metal engine is kept at the same level as in the two quartz engines, the combustion is much shorter in duration in the MSB than in the QSB.

Figure 13 shows that the in-cylinder pressures during LES agree well in all three cases with results of the experiments. The motored run pressure traces of the three piston engines are similar since the compression ratios and engine configurations are likewise.

A characteristic heat release rate HR^* for LES can also bee seen in the figures, where $HR^* \equiv d\overline{c} \,/\, d\,\mathrm{CAD}$, and $\overline{c}$ is the reaction progress variable averaged over the entire cylinder volume. The significant heat release in the of case QD starts at TDC and lasts until about 15 CAD. The duration of combustion is defined as the time between 10 % and 90 % heat release ($\overline{c} = 0.1$ to $\overline{c} = 0.9$) which is about 10 CAD.

Figure 14 shows an instantaneous temperature field at –300 CAD for two cross-sections, in the one a vertical plane intersecting the center of the piston bowl and in the other one a horizontal plane being involved, located close to the engine head. In addition, a three-dimensional plot of the streamlines is provided the purple lines, showing the helical swirling/tumble flow motion and showing in orange, the iso-surface of the second eigenvalues of the velocity gradient tensor (the so-called lambda-2 [127]) the turbulence eddy structures. Stronger turbulence eddies can be seen in the proximity of the two intake ports, shown in green, and less in the bowl at this particular CAD in the intake stroke.

The temperature field is irregular and inhomogeneous. Careful examination of the temperature and turbulence field reveals that the two fields are closely coordinated with on another. The turbulence eddies enhance the heat transfer from the hot wall to the cold intake gases during the intake stroke.

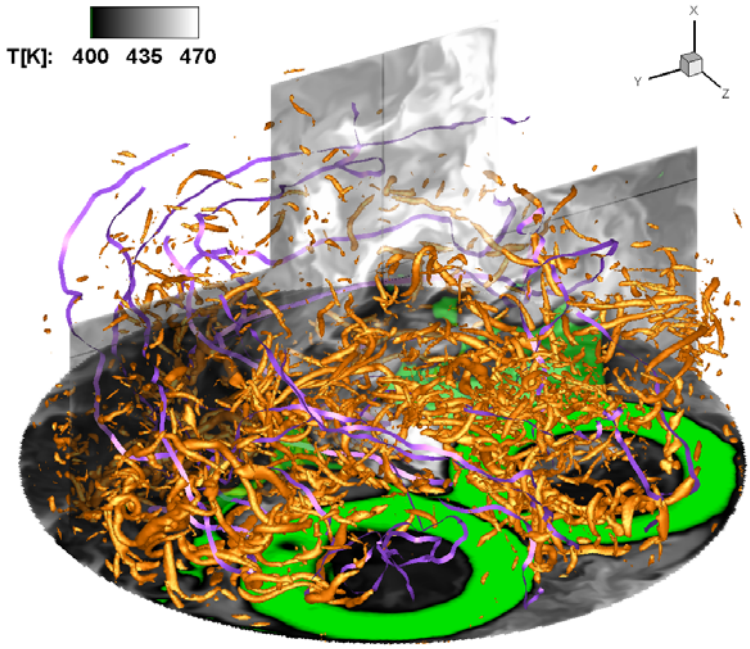

Figure 14: Instantaneous temperature field (on the two cross sections), flow streamlines (purple helical lines), and turbulence eddy structures (orange filament shape structures) at –300 CAD, obtained using LES.

The turbulence also enhances mixing of the cold intake gas and the hot residual gas. At –70 CAD in the compression stroke, figure 15, the region close to the surface for each of the two quartz pistons has the highest temperature, the hotter piston walls there heating up the gas in the vicinity. For the bowl of QSB in particular, the gas temperature is about 100 K higher within the bowl than in the squish zone. This explains why auto-ignition starts first in the bowl, as can be seen in the PLIF and chemiluminescence images. For the MSB, the gas temperature in the bowl is also higher, although the temperature difference is about 50 K less than in the QSB.

At –70 CAD and thereafter, the residual gas is rather well mixed with the intake gas in the entire cylinder. The higher gas temperature in the bowl is due to the larger surface-to-volume ratio there, not to the trapping of residual gas in the bowl. The residual gas stratification thus has no appreciable effect the onset of auto-ignition in these cases.

Both the temperature stratification and the intensity of the turbulence can be characterized by use of two statistical quantities: the turbulent fluctuation velocity u' and the temperature fluctuation T'. At each CAD, the instantaneous velocity field is first spatially filtered by means of a Gaussian filter having the filter size of the turbulence integral scale, estimated to be one-tenth of the bore. The filtered large-scale mean-flow retains the main tumble and swirl-motion. The temperature field is averaged over the volume as a whole so as to obtain the mean temperature for the cylinder. u' is defined as the root-mean-square of the difference between the local instantaneous velocity and the local filtered mean velocity and is averaged over the volume in its entirely. T' is defined in a corresponding way [38].

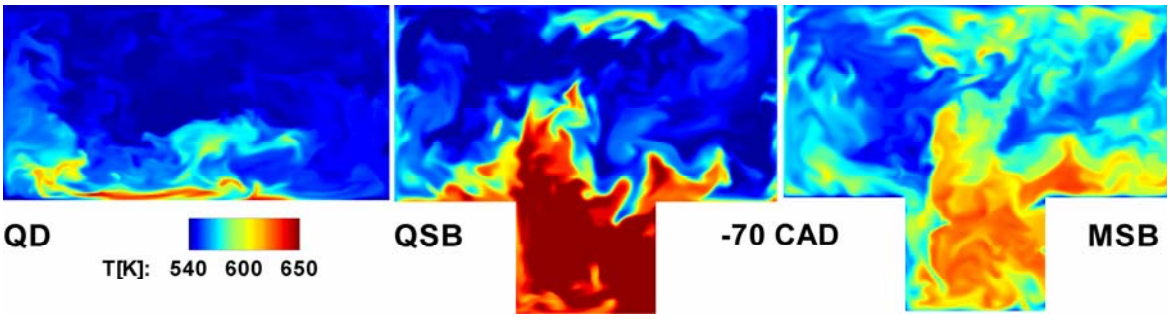

Figure 15: Instantaneous temperature distribution in the three engines at -70 CAD obtained using LES.

Figure 16 shows that the three cases are nearly identical in the value of u' during the intake and the early compression stroke. A rapid initial increase in u' takes place during the intake stroke, due to the strong shear flow from the intake gas. This can also be seen in figure 14. Since the structure of the intake flow is fairly independent of the piston shape, u' is virtually the same in all three cases. Later, in the compression stroke, the production of turbulence in the shear layer, that the bowl gives rise to, leads to a slight increase in u' in the case of QSB and MSB. This indicates that turbulence eddies may not be directly responsible for the increase in the combustion duration found for QSB case.

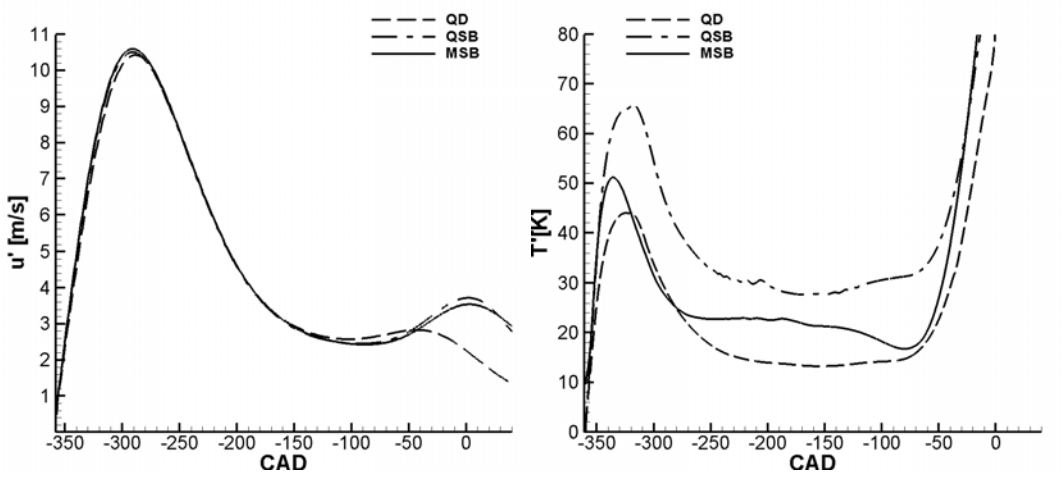

(a) (b)

Figure 16: (a) Evolution of u′ in the three engines, obtained using LES; (b) evolution of T′ in the three engines, obtained using LES.

QSB and QD, differ significantly however, in regard to the inhomogeneity in temperature that develops, as can be seen in figure 16b. The inhomogeneity in temperature is generated in the intake and compression stroke, due to turbulent transfer of heat between the hot walls and the bulk flow. When the surface-to-volume ratio in QSB is larger, the in-cylinder gas receives more heat from the walls. Thus, the temperature of the intake gas in QSB is set to a lower level then in QD, so as to maintain the same combustion phasing in both cases. The piston geometry and the turbulence intensity in MSB and in QSB, are virtually the same, as can be seen in figure 16a. However, since the piston wall is cooler in MSB than that in QSB, and the heating from the wall to the charge is less than that in QSB, the intake temperature has to be higher in MSB than that in QSB so as to maintain the same combustion phasing in both cases. However, because of T' being larger in QSB, its maximum in-cylinder temperature at late compression is still higher than that in QD and MSB, and its lowest temperature is lower than the corresponding ones for QD and MSB. This explains the longer combustion duration observed in QSB. Further information regarding the investigation is to be found in Paper 1 in the appendix.

5.2 Effect of Turbulence on HCCI combustion

In the previous section it was observed that the onset of auto-ignition kernels in homogeneous charges is governed by the temperature stratification, and that turbulence plays an important role in the development of temperature stratification in the cylinder. Direct interactions between turbulence and the ignition front are not well understood however. To obtain a better understanding of the ignition process and its dependence upon turbulence and on the temperature field numerical simulations of ethanol/air combustion, using a relative air/fuel ratio (lambda) of 3.3 under idealized HCCI engine conditions, and a prescribed temperature field making use of two-dimensional sine waves to describe the hot and cold spots, was carried out with use of different modeling approaches. Specifically multi-zone simulation, which neglects the effects of flow on chemical reactions [128], and the large-eddy

simulation approach, making use of the reaction-progress-variable-tabulation-model discussed in Chapter 3. Detailed chemical reaction mechanisms [126] are used in the simulations. Systematic investigation of the hot/cold spots involving use of different lengths and different amplitudes of temperature stratification were carried out. The initial field was set at 340 CAD. The initial turbulence field and pressure field were obtained from LES, the same engine configuration, fuel, and operating conditions as in the Scania D12 engine discussed in the previous section being employed. The initial temperature at 340 CAD is shown in the first column of figure 17 below.

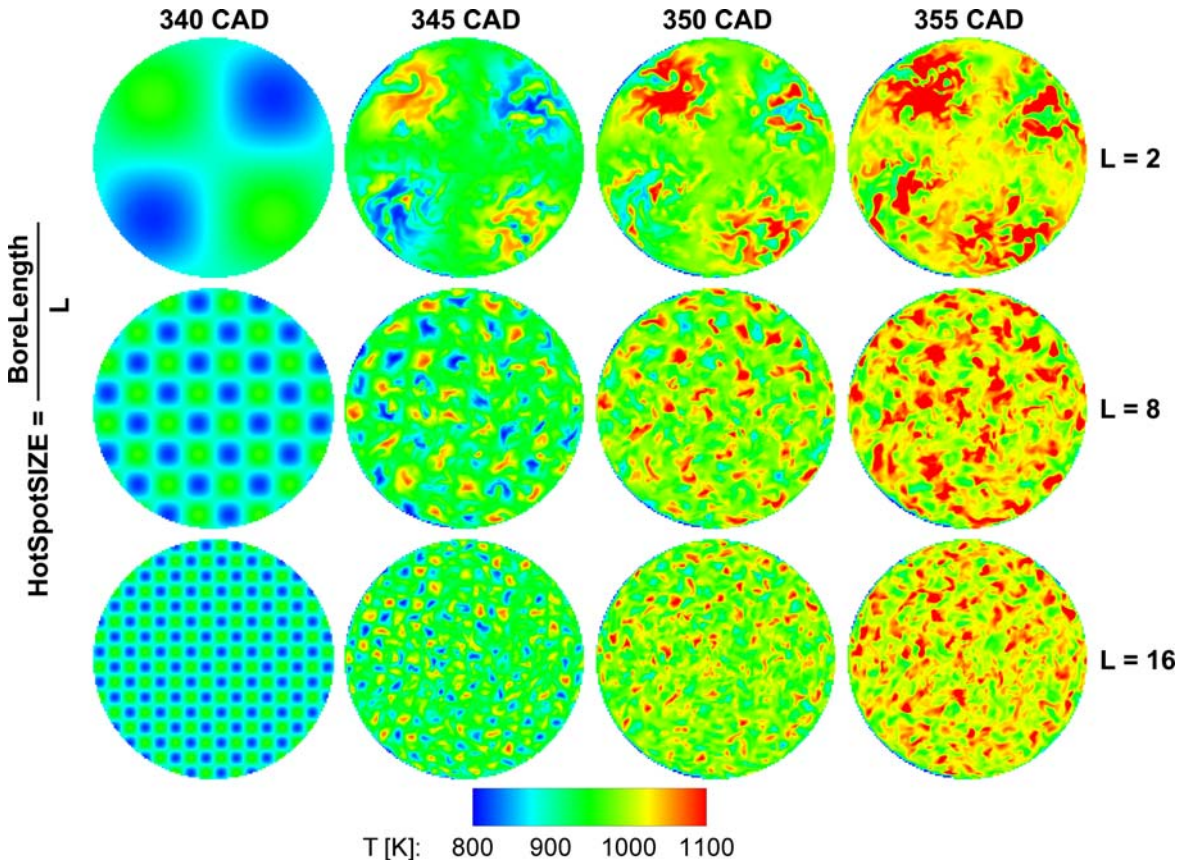

Figure 17: Temperature field in a cross-axis section at different crank angles, showing the ignition of hot spots of differing diameter. The initial variance in temperature is T'=35K. First row: initial hot/cold spot size at one-half of the bore length; second row: initial hot/cold spot size at one-eighth of the bore length; third row: initial hot/cold spot size at one-sixteenth of the bore length

Figure 17 shows three ignition events, the first one with a large hot spot size about half the size of the bore, the second one of smaller size, about one-eighth the bore in size, and the last one having an even smaller hot spot size, about one-sixteenth of the bore length. Regarding the effects of temperature stratification on HCCI combustion, it was found that at higher temperature stratification the mixture became easier to auto-ignite, so that under similar mean-temperature and flow conditions, auto-ignition occurs earlier, there and the combustion is of shorter duration, as can be seen in figure 18.

LES with use of the reaction progress variable model can simulate properly the effects of turbulence on the HCCI combustion process. The LES results indicates that under certain conditions the length scale of the stratified temperature field can play an important role in the auto-ignition process, cf. figure 18. It was also found that for a given initial mean temperature and level of stratification, smaller hot spots tender to auto-ignite then larger ones, due to their being smeared more by turbulent-eddy-transport.

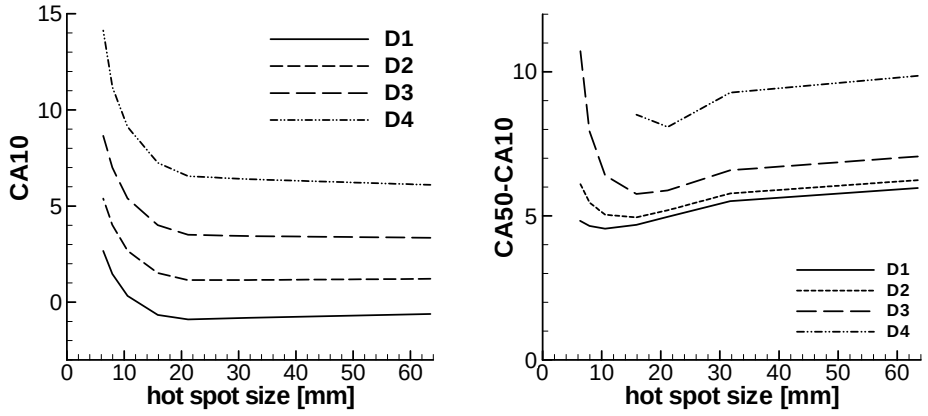

Figure 18: Combustion phasing (CA10) and duration (CA50 - CA10) of the hot spots for different sizes as predicted by LES. Mean temperature: 889K; Case D1: $T_0' = 49\text{K}$, D2; $T_0' = 42\text{K}$, D3; $T_0' = 35\text{K}$,D4; $T_0' = 28\text{K}$

It is of interest to note that for hot spots larger than the integral-scale large eddies the auto-ignition timing was rather insensitive to the size of the hot spots, cf. figure 18. In general, the combustion duration was less for smaller is than that of larger hot spots due to the smeared temperature field of the small hot spots leading to lesser temperature stratification. For very small hot spots, however, the auto-ignition occurs too late (after the piston has passed TDC). In such a case, expansion of the combustion chamber lowers the in-cylinder pressure and temperature, leading to slower combustion and also to incomplete combustion.

When the auto-ignition timing is held constant, combustion duration is found to be longer of larger then for smaller hot spots. This is due to the transport of hot gas from the combustion zone to the cold zone being less effective when a hot spot is large. This tendency trend is quite monotonic in character when the level of temperature stratification is high. When the level of temperature stratification is low (e.g. a low rms of the temperature) there is a particular hot spot size (in the order of the length of the eddies on the integral scale) tends to show faster combustion. This is the result of interaction between turbulence and the ignition front. Further details of the results obtained are presented in Paper 2.

5.3 Effect of Residual Gas on HCCI combustion

The effects of temperature and composition stratification on HCCI combustion was studied numerically by use of LES with calculation of the flow turbulence of the mixing process, and by use of a multi-zone method for simulating the ignition process and taking account of detailed chemical mechanisms. The simulations were carried out with use of a Volvo D5 engine of passenger car size, the ethanol fuel being supplied by means of port fuel injection. The temperature and composition stratifications in the engine cylinder were generated by use of a negative-valve-overlap (NVO) approach, which resulted in different levels of residual gas being trapped in the cylinder. In examining the effects of NVO on the mixing and ignition processes, the engine geometry and operational conditions were kept the same in all cases (e.g. the load, the residual gas temperature and the pressure at EVC and temperatures of the intake gas and the cylinder wall), only the valve timing (and thus the NVO) being varied.

Figure 19 shows the development of the temperature and concentration stratifications from LES. It was found that under all the NVO conditions the level of inhomogeneity of the composition was appreciable due to the residual gas mixed with the fresh intake fuel/air mixture remaining partly separate from each other up to the onset of ignition, the in-cylinder turbulence not being effective in fully mixing the two. This was indicated in part by the low scalar dissipation rate found for the compression stroke.

As can be seen in figure 20, there is a nearly linear relationship between the temperature and the distribution residual-gas mass-fractions – a high temperature tending to be associated with

a high residual-gas concentration, and vice versa, cf. figure 19. This is due to the similarity between process of the mixing of the residual gas with the fresh fuel/air mixture on the one hand, and the process of heat transfer between the hot residual gas and the comparatively colder fresh fuel/air mixture. These processes are governed by turbulence eddy interaction. The heat transfer process between the bulk flow, and the cylinder and the piston walls differ from the near-wall mixing of species, which leads to a departure of the temperature field from linear dependence upon the composition field at the low regions of temperature and low residual gas levels in the cylinder.

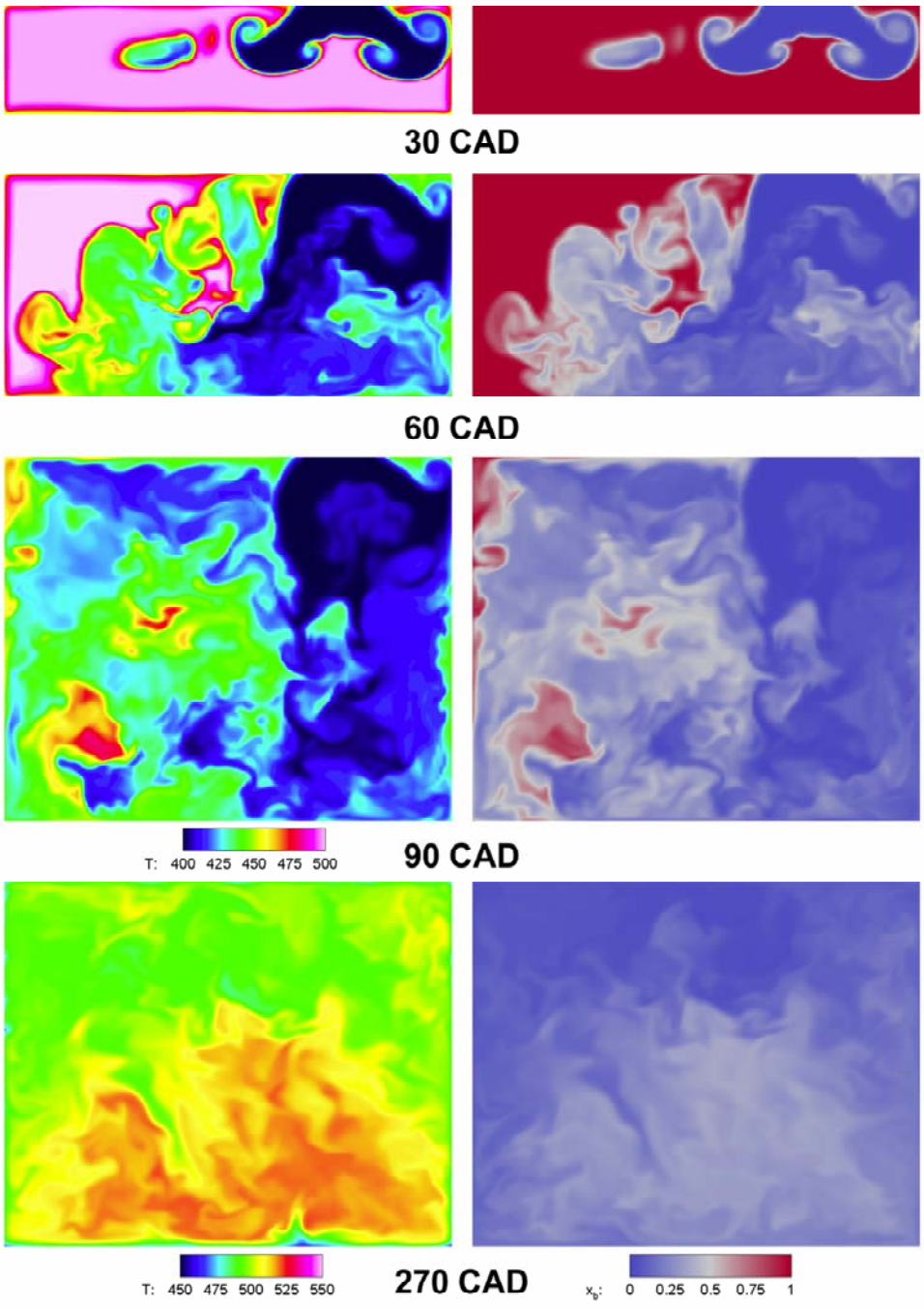

Figure 19: A sequence of LES resolved instantaneous fields for temperature (T, left column) and residual-gas mass fraction (x_b, right column) for the intake (30, 60 and 90 CAD) to the compression stoke (270 CAD). The plotted plane cuts through the cylinder axis.

For the low NVO cases (thus a low EGR rates) the ignition process in the mixtures involved was shown to depend more on the temperature than on the fuel concentration. For a high EGR rate (the NVO 160 case) there was a particular mixture and temperature level at which ignition occurred first.

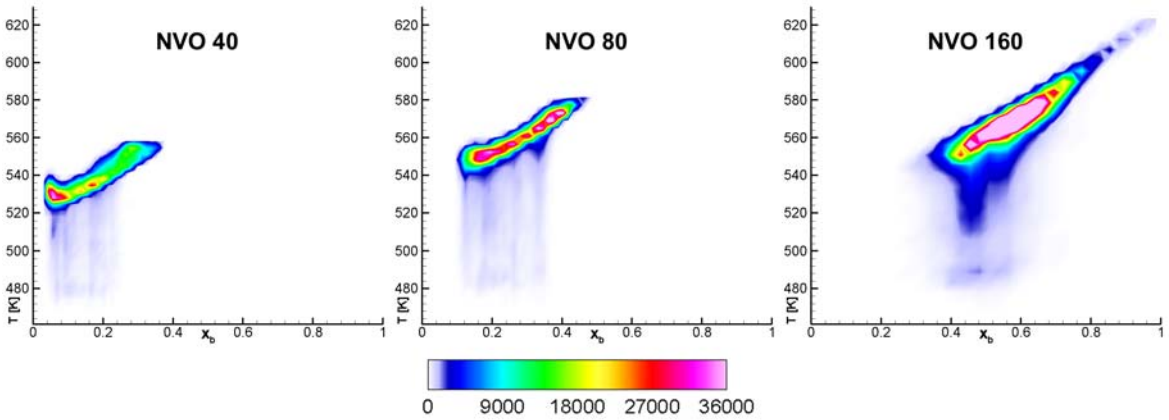

Figure 20: The joint PDF distribution for the temperature, T and the mass fraction of the residual-gas, x_b in (x_b,T) space at 290 CAD for the three NVO cases; the results are from LES.

Of the three NVO cases that were studied, the case involving an EGR rate of intermediate level (NVO 80 case) was found to have the earliest ignition. This was attributed to the compromises made in the NVO 80 case as compared with the other two cases between a higher in-cylinder gas temperature, on the one hand, and a lower EGR rate on the other. Further details regarding this study are to be found in Paper 3.

5.4 LES on temperature stratification in HCCI engines

It was found with use of LES and in the experiments discussed earlier that temperature stratification plays an important role in the HCCI combustion process. In order to better understand how temperature stratification develops in the engine, both LES and Laser-Induced-Phosphorescence (LIP) were carried out in an experimental Toyota engine that had a re-entrant-shaped piston. The engine experiments were performed within the KC-FP in collaboration with Toyota Motor. The studies were conducted under motored run conditions. The studies dealt with the onset of temperature stratification in the cylinders and with the sensitivity of temperature stratification and turbulence field to the inflow and the wall-boundary conditions.

Figure 21 shows for two different cases (2 and 3) the instantaneous turbulence eddies and the streamlines at different CAD. In both cases, the wall-temperature conditions were identical. For case 2, there was a swirl inlet whereas for case 3 there was no swirl at the inlet. This led to the development of different turbulence fields, rather different temperature fields in the cylinder.

The LES results enabled several different mechanisms responsible for the development of temperature stratification to be identified. One such mechanism was the mixing of the colder intake gas with the hotter residual gas in the cylinder, trapped there from the previous cycle. This was a source of temperature stratification at the beginning of the intake stroke. Another mechanism was heat transfer in the wall-boundary layer. In the later intake stroke, temperature stratification originated from heat-transfer between the bulk flow and the walls. It was found that the temperature stratification at this stage was rather constant, indicating there to be an equilibrium between the wall heat-transfer and turbulent mixing in the bulk flow (which always has a tendency to smear out the temperature stratification). A third mechanism was compression of the charge. In the compression stroke, the temperature stratification increases rapidly. This can be attributed mainly to the pressure increase that occurs which enhances the initial temperature gradients prior to compression.

In the compression stroke, this compression mechanism is the main source of temperature stratification. The wall heat-transfer that occurs further enhances the temperature stratification. For an adiabatic wall, therefore, no wall-heat-transfer occurred in the LES, lower temperature stratification being observed at TDC. In the expansion stroke, the temperature stratification decreases due to the compression mechanism and also to the turbulence mixing that occurs in the bulk flow.

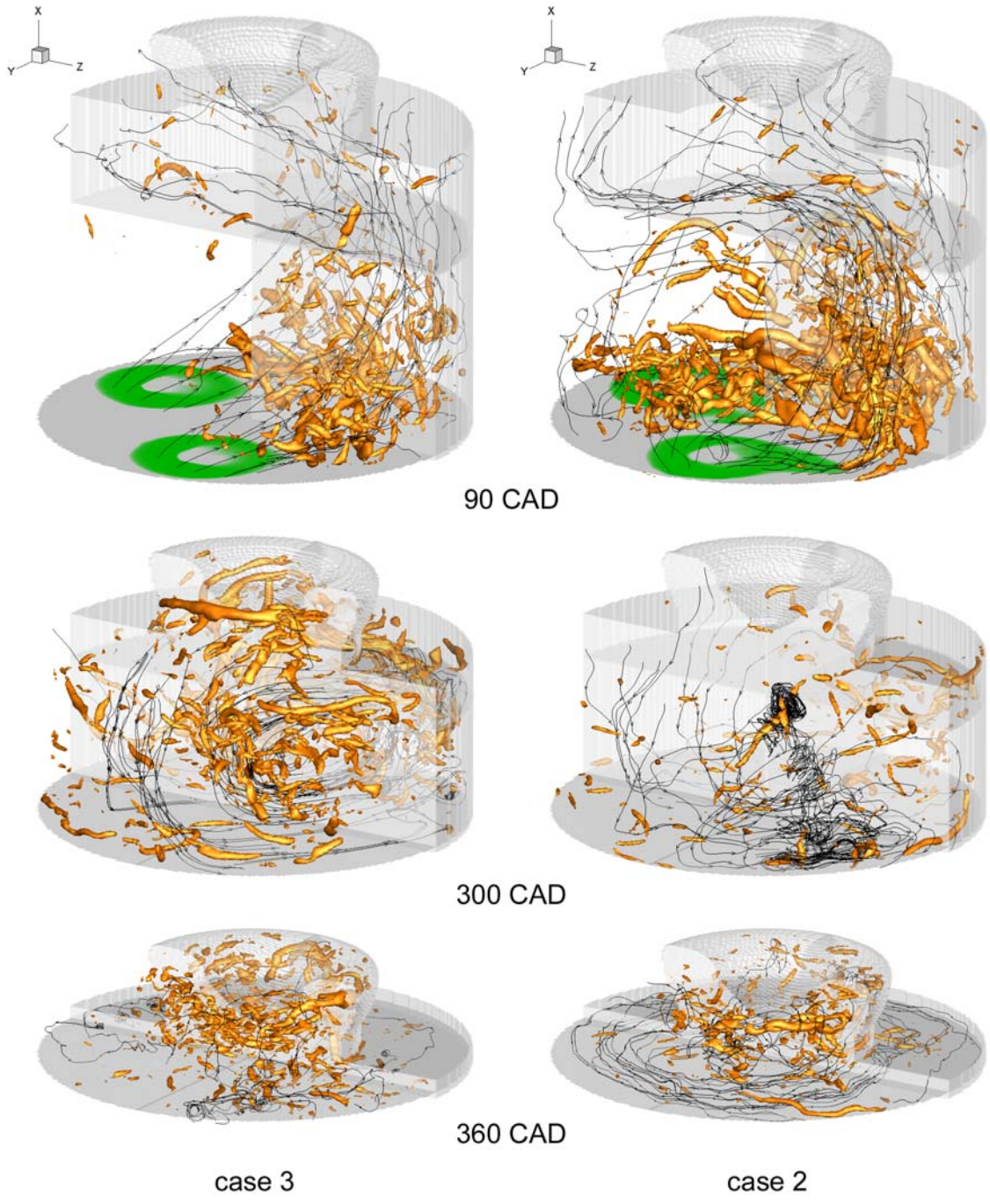

Figure 21: 3D iso-surfaces of the instantaneous λ_2 eigen-values of the velocity-gradient-tensor showing the turbulent eddy structures, and instantaneous streamlines showing the flow structures. The results are from LES for cases 2 and 3 at 90, 300, and 360 CAD. Further details concerning the cases are given in Paper 4 in the appendix.

It was found that large flow structures could also lead to temperature stratification, although this did not appear to be a dominant effect. This can be understood on the basis of the effects of inflow-swirl on the flow and temperature fields. The inflow-swirl is found to influence the main flow structures and the turbulence. The temperature stratification, on the other hand, seems to be rather similar in the cases of swirl and of non-swirl.

The piston-wall-temperature was shown to affect the temperature field and thus the in-cylinder pressure significantly, due to the major heat-transfer being between the piston walls and bulk flow in the compression stroke. Further details regarding this work can be found in Paper 4 in the appendix.

5.5 LES of spark-assisted HCCI combustion

Large Eddy Simulations of ethanol/air combustion in a HCCI engine were carried out to characterize the most suitable domains of operation for the HCCI, SI and SACI modes in practical engines. A LES SACI model is developed, as discussed earlier in Chapter 3. The model was used to study an experimental engine having a displacement volume in a cylinder of 480 cm^3 [129]. The engine ran at 1200 rpm and had a compression ratio of 12:1, a bore of 81 mm, and a stroke of 93.2 mm. The fuel employed was ethanol and it had an equivalence ratio of 0.61, its being supplied to the cylinder by port-fuel injection, enabling the fuel and air to mix well in the cylinder.

Figure 22 shows the development of the SI flame front (the dark solid line) and of the instantaneous temperature field at different crank angles for SACI-2. At 324 CAD, i.e., 4 CAD after the flame kernel was initiated in the middle of the cylinder. The flame kernel was found to be distorted from its initial spherical shape. The kernel was still at this time, rather small. Since the flame kernel was not appreciably larger than the resolved turbulence eddies were, the flame surface was not wrinkled. At 332 CAD, i.e. 12 CAD after the start-of-ignition, the flame kernel had grown larger and the flame surface displayed wrinkling. From 332 CAD to 359 CAD the SI premixed flame propagated from the central ignition site to become larger and highly wrinkled. As the premixed flame propagated and the piston moves to its TDC position the in-cylinder pressure increased due to compression and heat-release, which resulted in an increase in the temperature of the unburned charge outside the flame. At 359 CAD, no appreciable auto-ignition kernel was to be seen in the charge in the cross section shown. However, 3 CAD later, at 362 CAD, the charge had become auto-ignited at multiple sites outside the flame kernel, and 2 CAD later, at 364 CAD, most of the charge outside the flame kernel become ignited though rapid HCCI auto-ignition. The premixed flame front was seen to have propagated to the burned region after 362 CAD. This has no direct physical meaning, but rather serves to demonstrate the relative speed of ignition front propagation and flame front propagation.

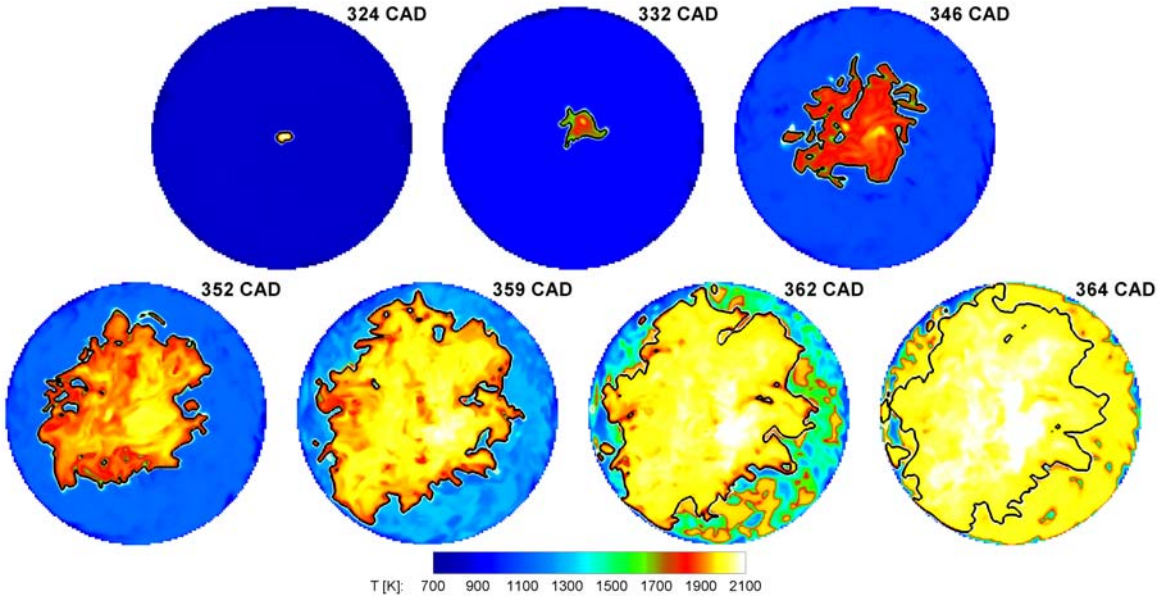

Figure 22: An instantaneous temperature field (on the 2D cut planes) showing the development of the SI flame front (enveloped by the black lines) and the HCCI ignition kernel (between the black lines and the cylinder walls) for a SACI test case.

SACI engine combustion can be divided up to two stages. From the LES results, it is seen that in the first stage of SACI combustion, between spark-ignition and the onset of HCCI auto-ignition, the turbulence field governs the heat-release-rate and the pressure-rise-rate in the cylinder. Increasing the turbulence promotes the contribution of SI flame to the overall heat release. The second stage of combustion, which is in the HCCI auto-ignition mode, is rather sensitive to the temperature field. The LES results showed that when the initial temperature is low the SI flame mode prevails, whereas when the initial temperature is high the HCCI mode prevails. At a moderate initial temperature, the SI flame and HCCI ignition interact more closely, this resulting in a higher degree of sensitivity to the initial temperature and turbulence conditions. This may possibly be the reason for the high degree of cycle variation found in the previous experiments [130].

5.6 LES of Tumble Flow and Turbulence in an Experimental Engine

LES is carried out to study in-cylinder turbulent flows in an experimental engine that has a simple rectangular shaped combustor geometry and a straight intake/exhaust channel. This test rig allows for detailed optical measurements of velocity field using PIV technique in a large window covering nearly the entire combustor. Boree et al. [131] used this setup to perform two dimensional velocity field for the symmetric plane of the chamber for more 100 cycles for different piston positions. The data were used to analyze the formation and breakdown of tumble flow in the intake stroke and the compression stroke using proper orthogonal decomposition (POD) technique [131]. Several authors have performed LES with this configuration to study the dynamics of tumble flow [132], and interesting phenomena such as cyclic variation [108].

The engine geometry is shown schematically in figure 23. The engine is of four-stroke type, running at a low speed of 206 rpm. The combustion chamber has a rectangular shape, with a width of b and a height of also b (b=100 mm). The intake channel has a width of b, a height of h (h=10 mm), and a length of 300 mm. The piston moves as a sinusoidal function of time as the following,

$$X_p(t) = 100 - 37.5\left[1 + \cos(6.87\pi t)\right] \quad [\mathrm{mm}]$$

where t=0 corresponds to the start of the intake, and X_p (=$a(t)$) is distance between the exit plane of the intake channel and the piston wall. The smallest X_p is 25 mm when the piston is at TDC. The largest X_p is 100 mm when the piston is at BDC. The maximum piston speed (V_p) is 0.809 m/s. The engine is operated in motored-run condition.

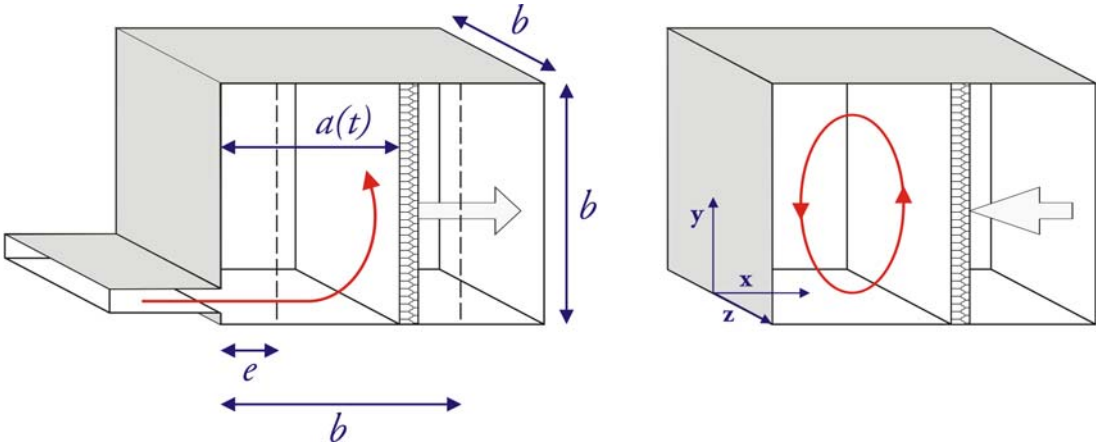

Figure 23: Sketch of the experimental rectangular engine.

The computational domain consists of both the rectangular combustion chamber and the intake channel. At the inlet of the intake channel a plug flow profile is used as the inflow

condition. The combustion chamber is described with a deforming grid of 128^3 cells, whereas the intake channel is simulated with a fixed grid of 128×72×72 cells in the x, y, z directions, respectively (cf. figure 23 for the definition of the coordinate system). With this grid and low engine speed, the average non-dimensional distance of the first grid to wall (y^+) in an engine cycle is about 5-15 in the width direction of the intake channel. In the vertical direction (y direction) y^+ is less than 2 in the intake channel. In the main chamber y^+ is about 1.2 – 5.4.

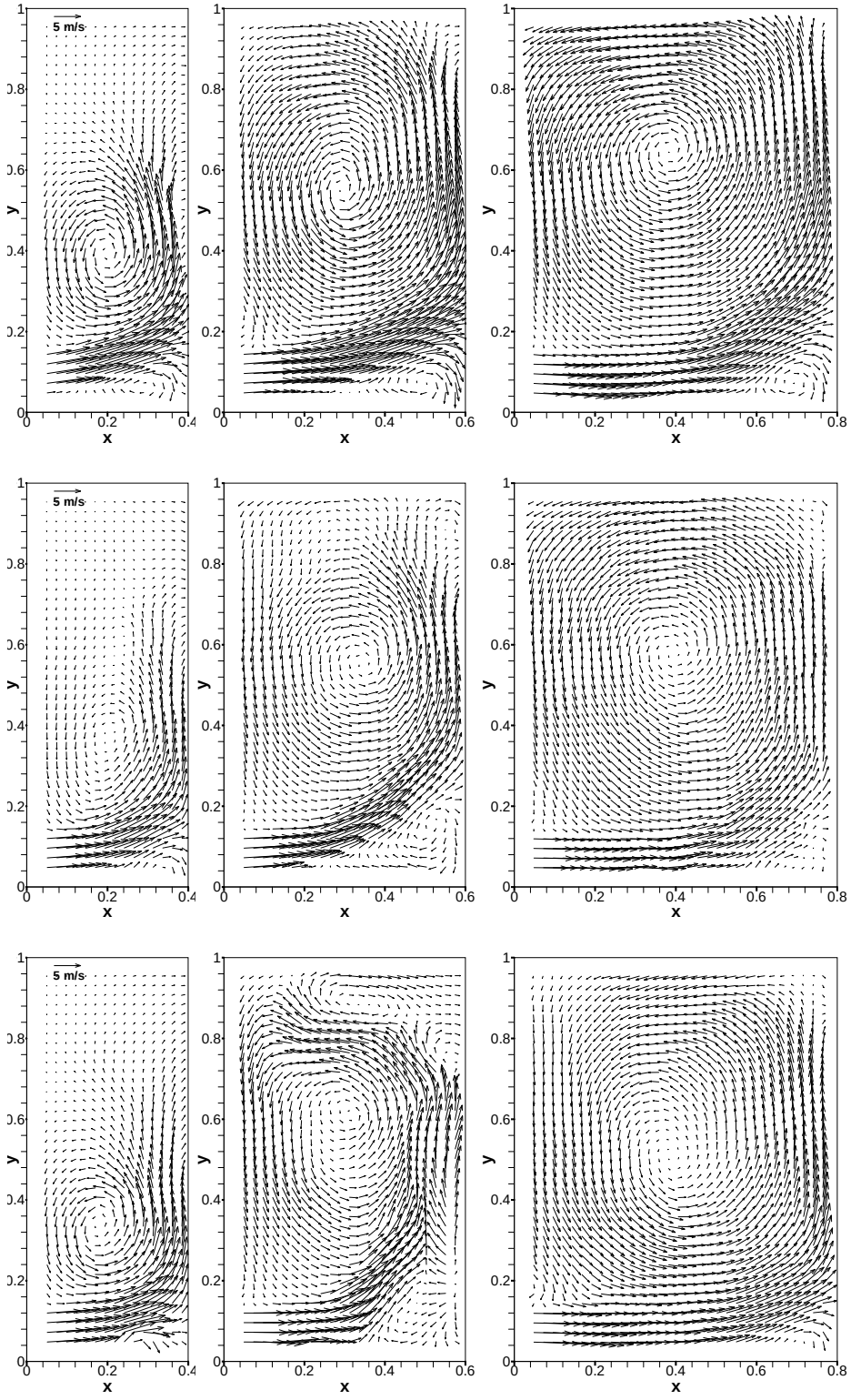

X_p = 40 mm X_p =60 mm X_p =80 mm

Figure 24: Cycle-averaged mean velocity vector field in the mid-z plane during the intake stroke. From left to right: X_p =40, 60 and 80 mm. First row: experiment; second row: LES1; third row: LES2. The axes were normalized with bore length b.

When the intake channel is simulated the mean flow at the exit plane of the intake channel develops to rather non-uniform; this may affect the incylinder turbulence and the mean flow in the combustion chamber. To investigate the effect of intake flow structure on the in-cylinder turbulence a simplified intake channel condition is employed, in which the intake channel is excluded from the numerical simulations. The inflow to the combustion chamber at the exit plane of the intake channel is modeled with a simple plug flow profile. These two LES runs are referred respectively to LES1 and LES2.

Figure 24 shows the cycle/ensemble-averaged statistical mean flow fields in the middle *z*-plane in three piston positions in the intake stroke. A large mean recirculation zone is formed in the geometric center of the combustion chamber, and in the low right corner a smaller corner recirculation zone is seen in both the experiments and LES1. In LES2, the results at X_p =60 mm in the intake stroke show two additional corner recirculation zone in the upper right corner of the chamber. This is different from the results of LES1 and the experiments. It is likely an effect of intake flow. It is found that the intake flow has relatively smaller impact on the in-cylinder flow in the compression stroke. Convergence of the cycle-averaged mean velocity and rms velocity is investigated. It is found that with 10 cycles the mean axial velocity is already converged; however, the rms velocity fluctuations still vary even when 60 cycles were used.

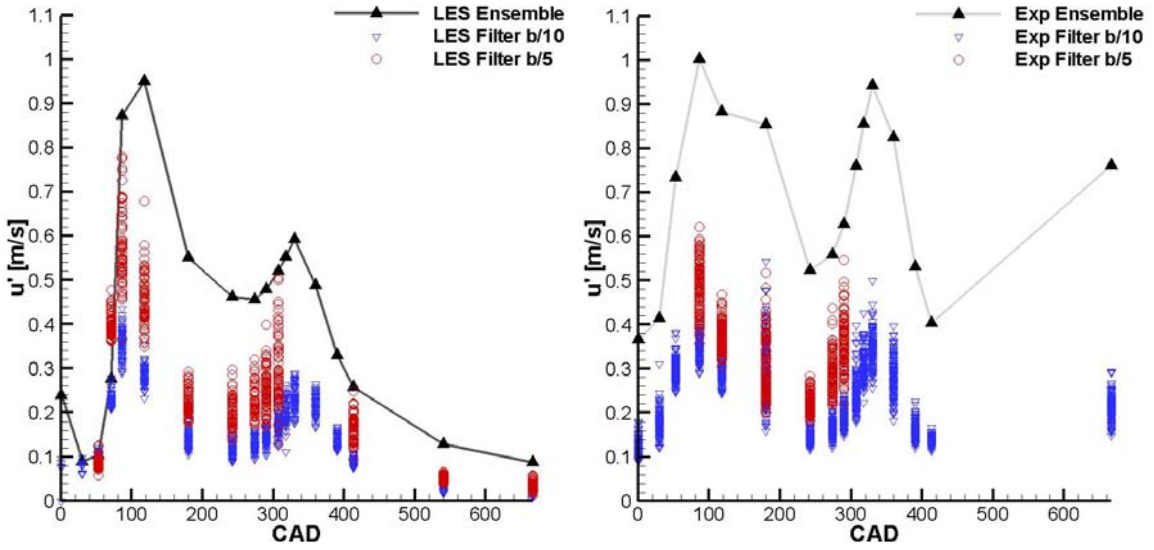

Figure 25: Cylinder averaged rms velocity at different CAD and cycles. (a) LES2, (b) Experiments.

Figure 25 shows the cylinder averaged global turbulence intensity (u_{TCA}). For comparison the cylinder averaged rms velocity fluctuation based on cycle/ensemble-averages are also plotted in the figure. It is seen that u_{TCA} increases rapid in the intake stroke as the piston moves away from the TDC position; the peak u_{TCA} is seen around CAD 100, where the intake flow velocity is also around its peak value. u_{TCA} decreases as the piston moves from CAD 100 to CAD 200, during which the piston speed decreases. In the compression stroke u_{TCA} increases and reaches its second peak around the TDC (CAD 360). Thereafter, u_{TCA} decreases in the expansion stroke. This variation of turbulence intensity is well known as discussed in [1]. It is seen that the results from LES2 and the experiments agree each other reasonably well.

From figure 25 it appears that u_{TCA} based on the spatial filtering of single cycle data can qualitatively describe the development and decay of incylinder turbulence in different strokes. With the filter size one tenth of the bore length, u_{TCA} is about 30% - 70% of the u_{TCA} based on cycle-averages. As discussed earlier, u_{TCA} based on cycle averages contains the contribution from both turbulence and cyclic variation, as such it is higher than the one based on spatial filtered single cycle data. Further details of the results are given in Paper 6 in the appendix.

Chapter 6 Conclusions and Future Work

LES was employed for studying HCCI combustion under varying engine-operation and mixture conditions, including real engine configurations and generic test cases. The fuel considered was ethanol, since the engine experiments available involved use of ethanol. Effect of the combustor geometry and of turbulence on HCCI combustion was studied, the development of turbulence and of temperature stratification in different engines being investigated. A new SACI combustion model was developed and was used to study SI flame propagation and the interaction between SI flame and HCCI ignition-front propagation. The major conclusions drawn can be summarized to follows.

HCCI combustion is strongly affected by in-cylinder temperature stratification. For a given combustion phasing, e.g. a particular CA10, in which there is considerable temperature stratification, both the combustion process and the pressure-rise-rate are slower, making it possible to run the engine at a high load level.

Turbulence can affect the HCCI combustion process under various conditions in particular. Under typical engine conditions, due to rapid propagation of the ignition front, turbulence cannot affect the reaction zones directly, such as through wrinkling of the reaction front or through differential diffusion that serves to adjust the radical levels. Turbulence affects HCCI combustion mainly by modifying the temperature field. It affects the combustion process in two ways. One of these is by generating temperature stratification through heat transfer between the wall and the in-cylinder gas. The other way is to through its smearing out the temperature stratification in the gas mixture through the turbulence eddy action which is produced. If the hot zone or the cold zone in the mixture is large in size, e.g. larger than the integral length scale, turbulent heat transfer may fail to wipe out the temperature stratification quickly, the effect that turbulence has on the ignition process thus being less. At the same time if the scales of the hot/cold zones are small, turbulence can affect the HCCI combustion process appreciably nevertheless.

The temperature stratification that occurs is primarily generated by three different mechanisms: mixing of the cold intake gas with the hot residual gas, wall-heat transfer, and compression of the mixture. The last mechanism is less well known then the other two. The presence of large amounts of residual gas or EGR in the cylinder can serve to enhanced the temperature stratification due to the effects of the first mechanism.

Spark-assisted HCCI combustion is sensitive to both turbulence and temperature stratification. The operation window for SACI can be rather narrow, in that if the temperature is low the process involves mainly SI, and if the temperature is high, it involves mainly HCCI. It has been shown, however, that if the temperature is moderate, that the combustion process is rather sensitive to changes in both the turbulence field and the temperature field. As a result, using SACI to control an HCCI engine may not be easy.

HCCI combustion has been shown to be sensitive to the temperature field. There is a need for methods being developed for generating desirable forms of temperature stratification in the cylinder making stable operation of HCCI engines possible. Another way of controlling HCCI combustion is to provide for concentration stratification either by injecting fuel into to the cylinder directly or by using large EGR. This is known as partially Premixed Charge Compression Ignition (PCCI). The reaction structures and dynamics of PCCI combustion are not well understood. The present LES HCCI models should be further improved and be validated regarding their applicability to mixtures having concentration stratification.

Acknowledgements

Firstly and foremost thanks to my main-supervisor, professor Xue-Song Bai to first open the opportunity for me to conduct Ph.D. studies. He always took time to show me around in the fantastic world of Fluid Dynamics, Combustion and LES. He also taught me that it is not over until it is over, and not even then it is over.

Then thanks to Rixin, who at times and times explained to me how the code worked and what we actually were looking at by using a pencil and a notebook.

Thanks too my co-supervisor, professor Bengt Johansson, who helped me to grab the feeling of how a engine works and sounds like "in the so known real life".

Thanks to the people at Fluid Mechanics Division who made it fun to go back to the office, when I occasionally had to leave it. Kalle, as the man who showed how me how you can live with LES, together with a life including other matters. Piero, who listen to quadruple opened parentheses and still be able to become the most behaved and structured one, at least in his room. Holger, for visualizing how you can combined Fluid Mechanics with beer, and by saving his office from burning down and by that saving this thesis from being destroyed in the flames. Eric, who always find a fix point in a highly turbulent environment. Jiangfei, for also enjoy staying in the office, and as me be there at all timesteps on days and nights, every weekday. And to Mehdi, Henning, Rickard, Hesam, Aurélia, Fan, Julien, Alper, Yajing, Christian, Johan, Robert, Laszlo and Dragan.

Thanks to my additional co-writers who I did write papers with, and to talk to, Noriyuki, Johan, Johannes, Marcus, Mattias, Andreas and Per. Thanks to Esteban for teaching me to value the connecting points in life.

Thanks to my family who supported me in my flowing interests of exploration.

The thesis was proudly sponsored by the Swedish Research Council, VR the Swedish Energy Agency through KC-FP. Whereas for the provider of the huge computational resources stands LUNARC and HPC2N.

References

1. J.B. Heywood, "Internal Combustion Engine Fundamentals", McGraw-Hill, (1988)
2. F. Zhao, T.W. Asmus, D.N. Assanis, J.E. Dec, J.A. Eng, P.M. Najt, "Homogeneous Charge Compression Ignition (HCCI) Engines: Key Research and Development Issues", Society of Automotive Engineers, Inc., (2003)
3. B. Johansson, "Förbränningsmotorer"
4. I. Glassman, "Combustion" 2 edn., Academic Press Inc., (1987)
5. J. Nygren, J. Hult, M. Richter, M. Aldén, M. Christiansen, A. Hultqvist, B. Johansson, "Three-dimensional Laser Induced Flourescence of Fuel Distribution in an HCCI Engine" **Proceedings of the Combustion Institute** Vol. 29 pp. 679-685 (2002)
6. N. Peters, "Turbulent Combustion", Cambridge University Press, (2000)
7. T. Poinsot, D. Veynante, "Theoretical and Numerical Combustion", R.T. Edwards, (2001)
8. S.B. Pope, "Turbulent Flow", Cambridge University Press, (2000)
9. H. Persson, "Spark Assisted Compression Ignition SACI", **Doctoral Thesis**, Department of Energy Sciences, Lund University (2008)
10. T. Kamimoto, M.-H. Bae, "High Combustion Temperature for the Reduction of Particulate in Diesel Engines" **SAE 880423** (1988)
11. H. Zhao, "HCCI and CAI engines for the automotive industry", Woodhead Publishing Limited, (2007)
12. S. Onishi, J. Hong, K. Shoda, P.J. Do, S. Kato, "Active thermoatmosphere combustion ATAC - A new combustion process for internal combustion engines" **SAE 790507** (1979)
13. M. Noguchi, Y. Tanaka, T. Tanaka, Y. Takeuchi, "A study of gasoline engine combustion by observation of intermediate reactive products during combustion" **SAE 790840** (1979)
14. P.M. Najt, D.E. Foster, "Compression-Ignited Homogeneous Charge Combustion" **SAE 830264** (1983)
15. A. Hultqvist, "Characterization of the Homogenous Charge Compression Ignition Combustion Process", **Doctoral Thesis**, Department of Heat and Power Engineering, Lund University (2002)
16. N. Iida, "Combustion Analysis of Methanol-Fueled Active Thermo-Atmosphere Combustion (ATAC) Engine Using a Spectroscopic Observation" **SAE 940684** (1994)
17. N. Iida, T. Ichikura, K. Kase, Y. Enomoto, "Self-ignition and combustion stability in a methanol fueled low heat rejection ceramic ATAC engine - analysis of cyclic variation at high wall temperatures and lean burn operation" **JSAE Review** Vol. 18:3 pp. 233-240 (1997)
18. N. Iida, "A Study of Autoignition and Combustion in Two-Stroke ATAC Engine - Compression Ignition Characteristics of Low Carbon Alternative Fuels" **SAE 1999-01-3274** (1999)
19. H. Oguma, T. Ichikura, N. Iida, "Adaptability of gasoline, methanol, methane fuels to lean burn in an ATAC engine" **Nippon Kikai Gakkai Ronbunshu, B Hen/Transactions JSME, Part B** Vol. 63:613 pp. 3150-3157 (1997) [Japanese]
20. P. Duret, S. Venturi, "Automotive Calibration of the IAPAC Fluid Dynamically Controlled Two-Stroke Combustion Process" **SAE 960363** (1996)

21. M. Christensen, B. Johansson, P. Einewall, "Homogeneous Charge Compression Ignition (HCCI) Using Isooctane, Ethanol and Natural Gas - A Comparison with Spark Ignition Operation" **SAE 972874** (1997)
22. M. Christensen, B. Johansson, P. Amnéus, F. Mauss, "Supercharged Homogeneous Charge Compression Ignition" **SAE 980787** (1998)
23. M. Christensen, B. Johansson, "Influence of Mixture Quality on Homogeneous Charge Compression Ignition" **SAE 982454** (1998)
24. M. Christensen, B. Johansson, "Homogeneous Charge Compression Ignition with Water Injection" **SAE 1999-01-0182** (1999)
25. M. Christensen, B. Johansson, "Supercharged Homogeneous Charge Compression Ignition (HCCI) with Exhaust Gas Recirculation and Pilot Fuel" **SAE 2000-01-1835** (2000)
26. M. Christensen, "HCCI Combustion - Engine Operation and Emission Characteristics", **Doctoral Thesis**, Department of Heat and Power Engineering, Lund University (2003)
27. M. Christensen, A. Hultqvist, B. Johansson, "The Effect of Combustion Chamber Geometry on HCCI Operation" **SAE 2002-01-0425** (2002)
28. M. Christensen, B. Johansson, "The Effect of In-cylinder Flow and Turbulence on HCCI Combustion" **SAE 2002-01-2864** (2002)
29. S.-C. Kong, R.D. Reitz, M. Christensen, B. Johansson, "Modeling the Effects of Geometry Generated Turbulence on HCCI Engine Combustion" **SAE 2003-01-1088** (2003)
30. J.-O. Olsson, "The HCCI Engine - High Load Performance and Control Aspects", **Doctoral Thesis**, Department of Heat and Power Engineering, Lund University (2004)
31. O. Stenlåås, "On the Impact of Piston Motion and In-Cylinder Charge Composition on Energy Release, Auto Ignition and Emission Formation in Premixed Charge Internal Combustion Engines", **Doctoral Thesis**, Department of Heat and Power Engineering, Lund University (2004)
32. J. Hyvönen, "The Performance of a Multi Cylinder HCCI Engine using Variable Compression Ratio and Fast Thermal Management", **Doctoral Thesis**, Department of Heat and Power Engineering, Lund University (2005)
33. L. Hildingsson, "Laser Diagnostics of HCCI and Partially Premixed Combustion", **Doctoral Thesis**, Department of Heat and Power Engineering, Lund University (2006)
34. P. Strandh, "HCCI operation - closed loop combustion control using VVA or dual fuel", **Doctoral Thesis**, Department of Heat and Power Engineering, Lund University (2006)
35. A. Vressner, "Studies on the Load Range of an HCCI Engine using In-Cylinder Pressure, Ion Current and Optical Diagnostics", **Doctoral Thesis**, Department of Energy Sciences, Lund University (2007)
36. V. Manente, "Gasoline Partially Premixed Combustion", **Doctoral Thesis**, Department of Energy Sciences, Lund University (2010)
37. T. Johansson, "Turbocharged HCCI Engine", **Doctoral Thesis**, Department of Energy Sciences, Lund University (2010)
38. R. Yu, "Large Eddy Simulation of Turbulent Flow and Combustion in HCCI Engines", **Doctoral Thesis**, Department of Energy Sciences, Lund University (2008)
39. L. Koopmans, I. Denbratt, "A Four Stroke Camless Engine, Operated in Homogeneous Charge Compression Ignition Mode with Commercial Gasoline" **SAE 2001-01-3610** (2001)

40. L. Koopmans, R. Ogink, I. Denbratt, "Direct Gasoline Injection in the Negative Valve Overlap of a Homogeneous Charge Compression Ignition Engine" **SAE 2003-01-1854** (2003)
41. L. Koopmans, J. Wallesten, R. Ogink, I. Denbratt, "Location of the First Auto-Ignition Sites for Two HCCI Systems in a Direct Injection Engine" **SAE 2004-01-0564** (2004)
42. A. Helmantel, I. Denbratt, "HCCI Operation of a Passenger Car Common Rail DI Diesel Engine With Early Injection of Conventional Diesel Fuel" **SAE 2004-01-0935** (2004)
43. L. Koopmans, E. Strömberg, I. Denbratt, "The Influence of PRF and Commercial Fuels with High Octane Number on the Auto-ignition Timing of an Engine Operated in HCCI Combustion Mode with Negative Valve Overlap" **SAE 2004-01-1967** (2004)
44. A. Helmantel, J. Gustavsson, I. Denbratt, "Operation of a DI Diesel Engine With Variable Effective Compression Ratio in HCCI and Conventional Diesel Mode" **SAE 2005-01-0177** (2005)
45. A. Berntsson, I. Denbratt, "Spark Assisted HCCI Combustion Using a Stratified Hydrogen Charge" **SAE 2005-24-039** (2005)
46. A. Helmantel, I. Denbratt, "HCCI Operation of a Passenger Car DI Diesel Engine with an Adjustable Valve Train" **SAE 2006-01-0029** (2006)
47. A. Berntsson, I. Denbratt, "HCCI Combustion Using Charge Stratification for Combustion Control" **SAE 2007-01-0210** (2007)
48. A. Berntsson, I. Denbratt, "Optical study of HCCI Combustion using NVO and an SI Stratified Charge" **SAE 2007-24-0012** (2007)
49. A. Berntsson, M. Andersson, D. Dahl, I. Denbratt, "A LIF-study of OH in the Negative Valve Overlap of a Spark-assisted HCCI Combustion Engine" **SAE 2008-01-0037** (2008)
50. D. Dahl, M. Andersson, A. Berntsson, I. Denbratt, L. Koopmans, "Reducing Pressure Fluctuations at High Loads by Means of Charge Stratification in HCCI Combustion with Negative Valve Overlap" **SAE 2009-01-1785** (2009)
51. G. Kalghatgi, P. Risberg, H.-E. Ångström, "A Method of Defining Ignition Quality of Fuels in HCCI Engines" **SAE 2003-01-1816** (2003)
52. P. Risberg, G. Kalghatgi, H.-E. Ångström, "Auto-ignition Quality of Gasoline-Like Fuels in HCCI Engines" **SAE 2003-01-3215** (2003)
53. P. Strålin, F. Wåhlin, H.-E. Ångström, "Effects of Injection Timing on the Conditions at Top Dead Center for Direct Injected HCCI" **SAE 2003-01-3219** (2003)
54. P. Risberg, G. Kalghatgi, H.-E. Ångström, "The Influence of EGR on Auto-ignition Quality of Gasoline-like Fuels in HCCI Engines" **SAE 2004-01-2952** (2004)
55. F. Agrell, H.-E. Ångström, B. Eriksson, J. Wikander, J. Linderyd, "Control of HCCI During Engine Transients by Aid of Variable Valve Timings Through the Use of Model Based Non-Linear Compensation" **SAE 2005-01-0131** (2005)
56. F. Agrell, H.-E. Ångström, B. Eriksson, J. Wikander, J. Linderyd, "Transient Control of HCCI Combustion by aid of Variable Valve Timing Through the use of a Engine State Corrected CA50-Controller Combined with an In-Cylinder State Estimator Estimating Lambda" **SAE 2005-01-2128** (2005)
57. P. Risberg, D. Johansson, J. Andrae, G. Kalghatgi, P. Björnborn, H.-E. Ångström, "The Influence of NO on the Combustion Phasing in an HCCI Engine" **SAE 2006-01-0416** (2006)
58. J.E. Dec, "Advanced compression-ignition engines - understanding the in-cylinder processes" **Proceedings of the Combustion Institute** Vol. 32 pp. 2727-2742 (2009)

59. M. Sjöberg, J.E. Dec, "An investigation into lowest acceptable combustion temperatures for hydrocarbon fuels in HCCI engines" **Proceedings of the Combustion Institute** Vol. 30:2 pp. 2719-2726 (2005)
60. P.L. Kelly-Zion, J.E. Dec, "A computational study of the effect of fuel type on ignition time in homogenous charge compression ignition engines" **Proceedings of the Combustion Institute** Vol. 28:1 pp. 1187-1194 (2000)
61. M. Yao, Z. Zheng, H. Liu, "Progress and recent trends in homogeneous charge compression ignition (HCCI) engines" **Progess in Energy and Combustion Science** Vol. 35 pp. 398-437 (2009)
62. M. Richter, J. Engström, A. Franke, M. Aldén, A. Hultqvist, B. Johansson, "The Influence of Charge Inhomogeneity on the HCCI Combustion Process" **SAE 2000-01-2868** (2000)
63. S.M. Aceves, D.L. Flowers, C.K. Westbrook, J.R. Smith, W. Pitz, R. Dibble, M. Christiansen, B. Johansson, "A Multi-Zone Model for Prediction of HCCI Combustion" **SAE 2000-01-0327** (2000)
64. A. Hultqvist, M. Christensen, B. Johansson, M. Richter, J. Nygren, J. Hult, M. Aldén, "The HCCI Combustion Process in a Single Cycle - Speed Fuel Tracer LIF and Chemiluminescence Imaging" **SAE 2002-01-0424** (2002)
65. Y.B. Zeldovich, "Regime Classification of an Exothermic Reaction with Nonuniform Initial Conditions" **Combustion and Flames** Vol. 39 pp. 211-214 (1980)
66. S. Hajireza, F. Mauss, B. Sundén, "Hot-spot autoignition in spark ignition engines" **Proceedings of the Combustion Institute** Vol. 28:1 pp. 1169-1175 (2000)
67. R. Sankaran, H.G. Im, "Characteristics of auto-ignition in a stratified iso-octane mixture with exhaust gases under homogeneous charge compression ignition conditions" **Combustion Theory and Modelling** Vol. 9:3 pp. 417-432 (2005)
68. R. Sankaran, H.G. Im, E.R. Hawkes, J.H. Chen, "The effects of non-uniform temperature distribution on the ignition of a lean homogeneous hydrogen–air mixture" **Proceedings of the Combustion Institute** Vol. 30:1 pp. 875-882 (2005)
69. J.H. Chen, E.R. Hawkes, R. Sankaran, S.D. Mason, H.G. Im, "Direct numerical simulation of ignition front propagation in a constant volume with temperature inhomogeneities I. Fundamental analysis and diagnostics" **Combustion and Flames** Vol. 145:1-2 pp. 128-144 (2006)
70. M. Kraft, P. Maigaard, F. Mauss, M. Christensen, B. Johansson, "Investigation of combustion emissions in a homogeneous charge compression injection engine: Measurements and a new computational model " **Proceedings of the Combustion Institute** Vol. 28:1 pp. 1195-1201 (2000)
71. S.M. Aceves, D.L. Flowers, J. Martinez-Frias, J.R. Smith, C.K. Westbrook, W. Pitz, R. Dibble, J.F. Wright, W.C. Akinyemi, R.P. Hessel, "A Sequential Fluid-Mechanic Chemical-Kinetic Model of Propane HCCI Combustion" **SAE 2001-01-1027** (2001)
72. D.L. Flowers, S.M. Aceves, J. Martinez-Frias, R.W. Dibble, "Prediction of carbon monoxide and hydrocarbon emissions in iso-octane HCCI engine combustion using multizone simulations " **Proceedings of the Combustion Institute** Vol. 29:1 pp. 687-694 (2002)
73. A. Vressner, A. Hultqvist, B. Johansson, "Study on Combustion Chamber Geometry Effects in an HCCI Engine using High-Speed Cycle-Resolved Chemiluminescence Imaging" **SAE 2007-01-0217** (2007)
74. A. Vressner, R. Egnell, B. Johansson, "Combustion Chamber Geometry Effects on the Performance of an Ethanol Fueled HCCI Engine" **SAE 2008-01-1656** (2008)
75. H. Seyfried, J. Olofsson, J. Sjöholm, M. Richter, M. Aldén, "High-Speed PLIF for Investigation of Turbulence Effects on Heat Release Rate in HCCI Combustion" **SAE 2007-01-0213** (2007)

76. R. Yu, X.S. Bai, A. Vressner, A. Hultqvist, B. Johansson, J. Olofsson, H. Seyfried, J. Sjöholm, M. Richter, M. Aldén, "Effect of Turbulence on HCCI Combustion" **SAE 2007-01-0183** (2007)
77. O. Lang, W. Salber, J. Hahn, S. Pischinger, K. Hortmann, C. Bücker, "Thermodynamical and Mechanical Approach Towards a Variable Valve Train for the Controlled Auto Ignition Combustion Process" **SAE 2005-01-0762** (2005)
78. J. Willand, R.-G. Nieberding, G. Vent, C. Enderle, "The Knocking Syndrome -Its Cure and Its Potential" **SAE 982483** (1998)
79. J. Lavy, J.-C. Dabadie, C. Angelberger, P. Duret, J. Willand, A. Juretzka, J. Schäflein, T. Ma, Y. Lendresse, A. Satre, C. Schultz, H. Krämer, H. Zhao, L. Damiano, "Innovative Ultra-low NOx Controlled Auto-Ignition Combustion Process for Gasoline Engines: the 4-SPACE Project" **SAE paper 2000-01-1837** (2000)
80. N.D. Wilson, A.J. Watkins, C. Dopson, "Asymmetric Valve Strategies and Their Effect on Combustion" **SAE 930821** (1993)
81. O. Reynolds, "An Experimental Investigation of the Circumstances Which Determine Whether the Motion of Water Shall Be Direct or Sinuous, and of the Law of Resistance in Parallel Channels" **Philosophical Transactions of the Royal Society of London** Vol. 174 pp. 935-982 (1883)
82. O. Reynolds, "On the Dynamical Theory of Incompressible Viscous Fluids and the Determination of the Criterion" **Philosophical Transactions of the Royal Society of London** Vol. 186 pp. 123-164 (1895)
83. H. Tennekes, J.L. Lumley, "A First Course in Turbulence", the MIT press, (1972)
84. A.N. Kolmogorov, "The Local Structure of Turbulence in Incompressible Viscous Fluid for Very Large Reynolds Numbers" **Doklady Akademii Nauk SSSR** Vol. 30:4 (1941) [Russian]
85. A.N. Kolmogorov, "The Local Structure of Turbulence in Incompressible Viscous Fluid for Very Large Reynolds Numbers" **Proceedings: Mathematical and Physical Sciences** Vol. 434:1890 pp. 9-13 (1991)
86. J. Klingmann, B. Johansson, "Interaction Between Turbulence and Flame in an S.I. Engine and in a Stationary Burner" **SAE 1999-01-0569** (1999)
87. S.A. Slimon, M.C. Soteriou, D.W. Davis, "Development of Computational Aeroacoutics Equations for Subsonic Flow Using a Mach Number Expansion Approach" **Journal of Computational Physics** Vol. 159:2 pp. 377-406 (2000)
88. G. Borman, K. Nishiwaki, "Internal-Combustion Engine Heat Transfer" **Progess in Energy and Combustion Science** Vol. 13:1 pp. 1-46 (1987)
89. R.S. Rogallo, P. Moin, "Numerical Simulation of Turbulent Flows" **Annular Review of Fluid Mechanics** Vol. 16 pp. 99-137 (1984)
90. J. Smagorinsky, "General Circulation Experiments with the Primite Equations" **Monthly Weather Review** Vol. 91:3 pp. 99-164 (1963)
91. S. Shaanan, J.H. Ferziger, W.C. Reynolds, "Numerical simulation of turbulence in the presence of shear ", Deptartment of Mechanical Engineering Stanford University, California, USA, (1975)
92. J.H. Ferziger, U.B. Mehta, W.C. Reynolds, "Large Eddy Simulation of Homogeneous Isotropic Turbulence" Symp on Turbul Shear Flows, Pennsylvania State University, University Park, PA, USA (1977)
93. O.J. McMillian, J.H. Ferziger, R.A. Rogallo, "Tests of Subgrid-Scale models in strained turbulence" **AIAA 80-1339** (1980)
94. M. Germano, "Turbulence: the filtering approach" **Journal of Fluid Mechanics** Vol. 238 pp. 325-336 (1992)
95. M. Germano, U. Piomelli, P. Moin, W.H. Cabot, "A dynamic subgrid-scale eddy viscosity model" **Physics of Fluids A** Vol. 3:7 pp. 1760-1765 (1991)

96. D.K. Lilly, "A proposed modification of the Germano subgrid-scale closure method" **Physics of Fluids A** Vol. 4:3 pp. 633-635 (1992)
97. J. Bardina, J.H. Ferziger, W.C. Reynolds, "Improved subgrid scale models for large eddy simulation" **13th Fluid and Plasma Dynamics AIAA Conference** Vol. AIAA-80-1357 (1980)
98. S. Liu, C. Meneveau, J. Katz, "On the properties of similarity subgrid scale model as deduced from measurements in a turbulent jet" **Journal of Fluid Mechanics** Vol. 275 pp. 83-119 (1994)
99. R. Yu, X.-S. Bai, H. Lehtiniemi, S.S. Ahmed, F. Mauss, M. Richter, M. Aldén, L. Hildingsson, B. Johansson, A. Hultqvist, "Effect of Turbulence and Initial Temperature Inhomogeneity on Homogeneous Charge Compression Ignition Combustion" **SAE 2006-01-3318** (2006)
100. Y. Zhang, B. Rogg, K.N.C. Bray, "2-D Simulation of Turbulent Autoignition with Transient Laminar Flamelet Source Term Closure" **Combustion Science and Technology** Vol. 105 pp. 211-227 (1995)
101. R.S. Cant, K.N.C.Bray, "A theoretical model of premixed turbulent combustion in closed vessels" **Combustion and Flames** Vol. 76 pp. 243-263 (1989)
102. G.M. Abu-Orf, R.S. Cant, "A turbulent reaction rate model for premixed turbulent combustion in spark-ignition engines" **Combustion and Flames** Vol. 122 pp. 233-252 (2000)
103. R. Yu, X.S. Bai, "LES of In-cylinder Turbulence and Temperature Stratification in a HCCI Engine" ECCOMAS Thematic Conference Compuational Combustion Delft, Netherlands (2007)
104. P. Schmitt, T. Poinsot, B. Schuermans, K.P. Geigle, "Large-eddy simulation and experimental study of heat transfer, nitric oxide emissions and combustion instability in a swirled turbulent high-pressure burner" **Journal of Fluid Mechanics** Vol. 570 pp. 17-46 (2007)
105. U. Piomelli, E. Balaras, "Wall-layer models for large-eddy-simulation" **Annular Review of Fluid Mechanics** Vol. 34 pp. 349-374 (2002)
106. C. Hasse, V. Sohm, B. Durst, "Detached eddy simulation of cyclic large scale fluctuations in a simplified engine setup" **International Journal of Heat and Fluid Flow** Vol. 30:1 pp. 32-43 (2009)
107. C. Hasse, V. Sohm, M. Wetzel, B. Durst, "Hybrid URANS/LES Turbulence Simulation of Vortex Shedding Behind a Triangular Flameholder" **Flow, Turbulence and Combustion** Vol. 83:1 pp. 1-20 (2009)
108. C. Hasse, V. Sohm, B. Durst, "Numerical investigation of cyclic variations in gasoline engines using a hybrid URANS/LES modeling approach" **Computers & Fluids** Vol. 39:1 pp. 25-48 (2010)
109. Y. Huang, V. Yang, "Dynamics and stability of lean-premixed swirl-stabilized combustion" **Progess in Energy and Combustion Science** Vol. 35 pp. 293-364 (2009)
110. J. Gullbrand, X.S. Bai, L. Fuchs, "High-order Cartesian grid method for calculation of incompressible turbulent flows" **International Journal for Numerical Methods in Fluids** Vol. 36 pp. 687-709 (2001)
111. R. Yu, K.-J. Nogenmyr, X.S. Bai, "LES of swirling turbulent methane/air flame" ECCOMAS thermatic conference on computational combustion, Lisbon, Portugal (2005)
112. A. Harten, B. Engquist, S. Osher, S.R. Chakravathy, "Uniformly high order accurate essentially non-oscillatory schemes. III" **Journal of Computational Physics** Vol. 71:2 pp. 231-303 (1987)

113. X.-D. Liu, S. Osher, T. Chan, "Weighted Essentially Non-Oscillatory schemes" **Journal of Computational Physics** Vol. 115:1 pp. 200-212 (1994)
114. G.-S. Jiang, C.-W. Shu, "Efficient Implementation of Weighted ENO Schemes" **Journal of Computational Physics** Vol. 126:1 pp. 202-228 (1996)
115. J.-Y. Yang, S.-C. Yang, Y.-N. Chen, C.-A. Hsu, "Implicit Weighted ENO Schemes for the Three-Dimensional Incompressible Navier-Stokes Equations" **Journal of Computational Physics** Vol. 146:1 pp. 464-487 (1998)
116. M. Salewski, "LES of Jets and Sprays Injected into Crossflow", **Doctoral Thesis**, Department of Heat and Power Engineering, Lund University (2006)
117. J.H. Ferziger, M. Peric, "Computational Methods for Fluid Dynamics" 3 edn., Springer Verlag, (2002)
118. J.C. Tannehill, D.A. Anderson, R.H. Pletcher, "Computational Fluid Mechanics and Heat Transfer" 2 edn., Taylor and Francis, (1997)
119. X.-S. Bai, "On the Modeling of Turbulent Combustion at Low Mach Numbers", **Doctoral Thesis**, Department of Mechanics, Royal Institute of Technology (1994)
120. J. Kim, P. Moin, "Application of a fractional-step method to incompressible Navier-Stokes equations" **Journal of Computational Physics** Vol. 59:2 pp. 308-323 (1985)
121. A.W. Cook, J.J. Riley, "Direct Numercial Simulation of a Turbulent Reactive Plume on a Parallel Computer" **Journal of Computational Physics** Vol. 129:2 pp. 263-283 (1996)
122. C.D. Pierce, "Progress-Variable Approach for Large-Eddy Simulation of Turbulent combustion", Stanford, (2001)
123. H.N. Najm, P.S. Wyckoff, O.M. Knio, "A Semi-implicit Numercial Scheme for Reacting Flow I. Stiff Chemistry" **Journal of Computational Physics** Vol. 143:2 pp. 381-402 (1998)
124. O.M. Knio, H.N. Najm, P.S. Wyckoff, "A Semi-implicit Numercial Scheme for Recating Flow II. Stiff, Operator-Split Formulation" **Journal of Computational Physics** Vol. 154:2 pp. 428-467 (1999)
125. B. Lessani, M.V. Papalexandris, "Time-accurate calculation of variable density flows with strong temperature gradients and combustion" **Journal of Computational Physics** Vol. 212:1 pp. 218-246 (2006)
126. N.M. Marinov, "A detailed chemical kinetic model for high temperature ethanol oxidation" **International Journal of Chemical Kinetics** Vol. 31:3 pp. 183-220 (1999)
127. J. Jeong, F. Hussain, "On the identification of vortex" **Journal of Fluid Mechanics** Vol. 285 pp. 69-94 (1995)
128. N. Peters, in: N. Peters, B. Rogg (Eds.), "Reduced kinetic mechanisms for applications in combustion systems" Lecture Notes in Physics Vol. 15 pp. 1-13, Chapter 1, Springer-Verlag (1993)
129. H. Persson, J. Sjöholm, E. Kristensson, B. Johansson, M. Richter, M. Aldén, "Study of Fuel Stratification on Spark Assisted Compression Ignition (SACI) Combustion with Ethanol Using High Speed Fuel PLIF" **SAE 2008-01-2401** (2008)
130. C.S. Daw, R.M. Wagner, K.D. Edwards, J. B. Green jr, "Understanding the transition between conventional spark-ignited combustion and HCCI in a gasoline engine" **Proceedings of the Combustion Institute** Vol. 31:2 pp. 2887-2894 (2007)
131. J. Borée, S. Maurel, R. Bazile, "Disruption of a compressed vortex" **Physics of Fluids** Vol. 14 (2002)
132. M.S. Toledo, L.L. Penven, M. Buffat, A. Cadiou, J. Padilla, "Large eddy simulation of the generation and breakdown of a tumbling flow" **International Journal of Heat and Fluid Flow** Vol. 28 pp. 113-126 (2007)

This page is intentionally left blank, almost.